2013

A 5 meter range non-planar CMUT array for Automotive Collision Avoidance

Jonathan Hernandez Aguirre
University of Windsor

A 5 meter range non-planar CMUT array for Automotive Collision Avoidance

By

Jonathan Hernandez Aguirre

A Thesis
Submitted to the Faculty of Graduate Studies
through Electrical and Computer Engineering
in Partial Fulfillment of the Requirements for
the Degree of Master of Science at the University of Windsor

Windsor, Ontario, Canada

2013

Library and Archives
Canada

Published Heritage
Branch

395 Wellington Street
Ottawa ON K1A 0N4
Canada

Bibliothèque et
Archives Canada

Direction du
Patrimoine de l'édition

395, rue Wellington
Ottawa ON K1A 0N4
Canada

Canadä

A 5 Meter Range Non-Planar CMUT Array for Automotive Collision Avoidance

by

Jonathan Hernandez Aguirre

APPROVED BY:

_____
. R. Rashidzadeh, Department of Electrical and Computer Engineering

_____
A. Riahi, Department of Mechanical, Automotive and Materials Engineering

_____
. S. Chowdhury, Advisor, Department of Electrical and Computer Engineering

May 17th 2013

DECLARATION OF ORIGINALITY

I hereby certify that I am the sole author of this thesis and that no part of this thesis has been published or submitted for publication.

I certify that, to the best of my knowledge, my thesis does not infringe upon anyone's copyright nor violate any proprietary rights and that any ideas, techniques, quotations, or any other material from the work of other people included in my thesis, published or otherwise, are fully acknowledged in accordance with the standard referencing practices. Furthermore, to the extent that I have included copyrighted material that surpasses the bounds of fair dealing within the meaning of the Canada Copyright Act, I certify that I have obtained a written permission from the copyright owner(s) to include such material(s) in my thesis and have included copies of such copyright clearances to my appendix.

I declare that this is a true copy of my thesis, including any final revisions, as approved by my thesis committee and the Graduate Studies office, and that this thesis has not been submitted for a higher degree to any other University or Institution.

ABSTRACT

A discretized hyperbolic paraboloid geometry capacitive micromachined ultrasonic transducer (CMUT) array has been designed and fabricated for automotive collision avoidance. The array is designed to operate at 40 kHz, beamwidth of 40˚ with a maximum sidelobe intensity of -10dB. An SOI based fabrication technology has been used for the 5x5 array with 5 sensing surfaces along each x and y axis and 7 elevation levels. An assembly and packaging technique has been developed to realize the non-planar geometry in a PGA-68 package.

A highly accurate mathematical method has been presented for analytical characterization of capacitive micromachined ultrasonic transducers (CMUTs) built with square diaphragms. The method uses a new two-dimensional polynomial function to more accurately predict the deflection curve of a multilayer square diaphragm subject to both mechanical and electrostatic pressure and a new capacitance model that takes into account the contribution of the fringing field capacitances.

DEDICATION

To my father Rogelio Hernandez Dominguez that with the work of their hands and the sweat of his brow showed me the right path to follow in life and made me the man I'm.

To my mother Maria de la Luz Aguirre Castaneda whose infinite love and understanding taught me to never stop enjoying the small things of the life.

To my beautiful country where I hope to return one day.

ACKNOWLEDGEMENTS

TABLE OF CONTENTS

LIST OF TABLES

LIST OF FIGURES

1 CHAPTER 1

INTRODUCTION

The research objective is presented in this chapter, the background of similar projects developed in the industry are presented to realize the need of a novel, cheap and reliable system that can meet the requirements of the industry. The basic working principle is presented to then justify the use of the CMUT in the development of the system. A brief explanation of some fabrication techniques used in the fabrication techniques is presented. The thesis organization is then covered.

1.1 *Goals*

1.1.1 *Research Objective*

The objective of this project is to develop, design and fabricate a CMUT (Capacitive Micromachined Ultrasound Transducer) array that will be used for collision avoidance and park assistant, being those air-coupled applications a mathematical model is needed to accurate calculate the necessary parameters that will dictate the behaviour of the array. Since is going to be used in the automobile the array needs to be designed considering the restrictions that this implied. A reliable and easy to implement fabrication and packaging process needs to be pursuit in order to facilitate the manufacturability of the array and reduce the cost involved.

1.1.2 *Background*

A collision avoidance system is an automobile safety system designed to reduce the severity of an accident. Also known as precrash system, forward collision warning system or collision mitigating system, use radar and sometimes laser and camera sensors to detect an imminent crash. Depending on the system they may warn the driver, precharge the brakes, inflate seats

for extra support, move the passenger seat, position head rests to avoid whip lash, tension seat belts and automatically apply partial or full braking to minimize impact.

In 2009 the U.S. National Highway Traffic Safety Administration (NHTSA) began studying whether to make frontal collision warning systems and lane departure warning systems mandatory. Several studies have been performed to introduce this technology in the market [1].

In 2011 a question has been submitted to the European Commission regarding stimulation of these "collision mitigation by braking" systems. The mandatory fitting of Advanced Emergency Braking Systems in commercial vehicles will be implemented on 1 November 2013 for new vehicle types and on 1 November 2015 for all new vehicles in the European Union [2]. This could, according to the impact assessment [3], ultimately save around 5 000 fatalities and 50 000 serious injuries per year across the EU.

In an important 2012 study [4] by the non-profit research organization, Highway Loss Data Institute, researchers examined how particular features of crash-avoidance systems affected the number of claims under various forms of insurance coverage. They found two crash-avoidance features provide the biggest benefits: (a) autonomous braking that would brake on its own, if the driver does not, to avoid a forward collision and (b) adaptive headlights that would shift the headlights in the direction the driver steers. Unexpectedly, they found lane departure systems to be not helpful, and perhaps harmful, at the first 2012 stage of development.

A collision avoidance system works basically as follows:

Different sensors installed in the vehicle constantly monitor their environment, so that can immediately detect those vehicles or obstacles that fall within the scope of range of the sensors.

When an object (vehicle, pedestrian, obstacle, etc.) is detected, the system determines whether the vehicle is in a situation that may occur imminent collision and, if so, is sent a first warning to the driver to perform a braking maneuver to avoid the impact.

If the driver doesn't react to the notice signals given, and the system detects that a collision is imminent if nothing is done, automatically slows the vehicle, so the impact can be avoided or at least reduce its severity.

Collision avoidance features are rapidly making their way into the new vehicle fleet. The most common new technologies include forward collision warning, autonomous braking, lane departure warning, lane departure prevention, adaptive headlights, blind spot detection, and back-up cameras.

Several companies have included those kinds of systems in their cars; different approaches to the problem have been taken:

Audi

The full version of the system (Pre-Sense Plus) works in four phases. In the first phase, the system provides warning of impending accident, while the hazard warning lights are activated, the side windows and sunroof are closed and the front seat belts are tensioned. In the second phase, the warning is followed by light braking, strong enough to win the driver's attention. The third phase initiates autonomous partial braking at a rate of 3 m/s². The fourth phase decelerates the car at 5 m/s² followed by automatic deceleration at full braking power, roughly half a second before projected impact.

A second system called (Pre-Sense Rear) is designed to reduce consequences of rear end collisions. Sunroof and windows are closed, seat belts prepared for impact. The optional memory seats are moved forward to protect the car occupants.

The system uses radar and video sensors and was introduced in 2010 on the 2011 Audi A8 [5].

Ford

Ford's Collision Warning with Brake Support was introduced in 2009 on the Lincoln MKS and MKT and the Ford Taurus [6]. This system provides a warning through a Head Up Display that visually resembles brake lamps. If the driver does not react, the system pre-charges the brakes and increases the brake assist sensitivity to maximize driver braking performance.

Honda

Honda's Collision Mitigation Brake System (CMBS, although originally introduced with the initials CMS) introduced in 2003 on the Inspire [7] (and later in Acura, Honda's luxury brand in Canada and the United States) uses a radar-based system to monitor the situation ahead and provide automatic braking if the driver does not react to a warning in the instrument cluster and a tightening of the seat belts. The Honda system was the world's first production system to provide automatic braking. The 2003 Honda system also incorporated an "E-Pretensioner" which worked in conjunction with the CMBS system with electric motors on the seat belts. When activated, the CMBS has three warning stages. The first warning stage includes audible and visual warnings to brake. If ignored, the second stage would include the E-Pretensioner tugging on the shoulder portion of the seat belt two to three times as an additional tactile warning to the driver to take action. The third stage, in which the CMBS predicts a collision is unavoidable, includes full seatbelt slack take up by the E-Pretensioner for more effective seat belt protection, and automatic application of the brakes to lessen the severity of the predicted crash. The E-

Pretensioner would also work to reduce seatbelt slack whenever the brakes are applied and the brake assist system is activated.

Mercedes-Benz

Mercedes's Pre-Safe system was unveiled in the fall of 2002 at the Paris Motor Show on the 2003 S-Class. Using ESP sensors to measure steering angle, vehicle yaw and lateral acceleration and Brake Assist sensors to detect emergency braking, Pre-Safe can tighten the seat belts, adjust seat positions including rear seats (if installed), raise folded rear headrests (if installed) and close the sunroof if it detects possible collision (including rollover) [8]. A later version of Pre-Safe system was supplemented by an additional function that can close any open windows if necessary.

Pre-Safe Brake, Mercedes-Benz's first forward warning collision system was introduced in the fall of 2005 on the redesigned 2006 S-Class is co-operating with simultaneously introduced Brake Assist Plus and Distronic Plus systems and provides all the functions of previous Pre-Safe system while adding a radar-based system which monitors the traffic situation ahead and provides automatic partial braking (40% or up to 0.4g deceleration) if the driver does not react to the Brake Assist Plus warnings and the system detects a severe danger of an accident [8].

Toyota

Toyota Motor Corporation's Pre-Collision System (PCS), the first production forward warning collision system, is used on the manufacturer's Lexus and Toyota brand vehicles. It is a radar-based system which uses forward-facing millimeter-wave radar. When the system determines a frontal collision is unavoidable it pre-emptively tightens the seat belts removing any slack and

pre-charges the brakes using brake assist to give the driver maximum stopping power instantly when the driver depresses the brake pedal. Toyota launched PCS in February 2003 on the redesigned Japanese domestic market Harrier and in August 2003 added an automatic partial pre-crash braking system to the Celsior. In September 2003, PCS made its first appearance in North America on the Lexus LS 430, becoming the first such system offered in the US. In 2004, Toyota advanced the system by adding to the radar a single digital camera to improve accuracy of collision forecast and warning, control levels; it was first available on the Crown Majesta.

In 2006, the debut of the Lexus LS featured a further advanced version of the PCS; this newer version dubbed Advanced Pre-Collision System (APCS) added a twin-lens stereo camera located on the windshield and a more sensitive radar to detect for the first time smaller "soft" objects such as animals and pedestrians. A near-infrared projector located in the headlights allows the system to work at night. By using the LS's Adaptive Variable Suspension (AVS) and electric Variable Gear Ratio Steering (VGRS) the system can change the suspension damper firmness; steering gear ratios and torque assist to aid the driver's evasive steering measures in a system known as "Collision-avoidance Steering Support". The Lane Keep Assist system will make automatic steering adjustments to help ensure the vehicle maintains its lane in case the driver fails to react.

Also unveiled for the 2007 model year, the world's first Driver Monitoring System was introduced on the Lexus LS, using a CCD camera on the steering column; this system monitors the driver's face to determine where the driver is looking. If the driver's head turns away from road and a frontal obstacle is detected the system will alert the driver using a buzzer and if necessary pre-charge the brakes and tighten the safety belts. A later version of the Driver Monitoring System found in 2008 on the Crown monitors the driver's eyes to detect the driver's

level of wakefulness. This system is designed to work if the driver is wearing sunglasses and at night.

Other advancements to the PCS appearing on the 2007 Lexus LS include the first rearward-facing millimeter-wave radar mounted in the rear bumper. This system adjusts the active head restraints by moving them upward and forward to reduce the risk of whiplash injuries if an imminent rear collision is detected [9].

Based on the review of the state-of-the-art in collision avoidance system and considering the undeniable increase of those systems in the market an advanced and affordable collision avoidance system is being developed to attack this problem [10], [11] as shown in Figure 1-1
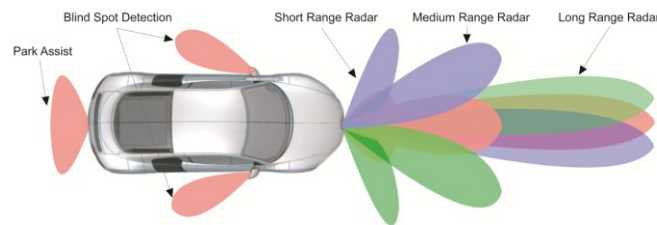
Figure 1-1 Ultrasonic sensors and radar for range detection and blindspot warning

A fundamental part of this system is the Blind Spot Detection sensor. A blind spot in a vehicle is an area around the vehicle that cannot be directly observed by the driver while at the controls, under existing circumstances. Blind spots exist in a wide range of vehicles: cars, trucks, motorboats and aircraft.

As one is driving an automobile, blind spots are the areas of the road that cannot be seen while looking forward or through either the rear-view or side mirrors. The most common are the rear quarter blind spots, areas towards the rear of the vehicle on both sides. Vehicles in the adjacent lanes of the road that fall into these blind spots may not be visible using only the car's mirrors.

Blind spot detection is critical for safe driving of vehicles during lane change maneuvers as the side view and rear view mirrors don't provide complete coverage of blind spots. A number of side impacts and rear-end collisions happen due to a driver's inability to monitor the blind spots. Some high-end vehicles use vision based sensors like camera or stand-alone ultrasonic sensors to monitor blind spots. Due to high cost, low-end vehicles don't have any blind spot detection system that can tell a driver if the lane change is safe or not. Cost-effective but high performance blind spot detection or monitoring system for automobiles is highly desirable to save lives and property damage.

The performance of current vision based systems for blind spot monitoring such as side view mirror mounted cameras or lasers are compromised in bad weather. Current technology of electromagnetic radars is too expensive and they need a rotating platform to scan the target area. Ultrasonic sensors are good for short range proximity detection. An array of ultrasonic sensors can be used to form a directional acoustical beam focused at the blind spot of a vehicle. These solutions and their variants require significant processing power to be implemented, adding to system cost, complexity and power requirements. The time delay associated with the intensive processing requirements limits the use of such beamformers in applications where real time implementation is crucial [12], [13].

In this context, piezoelectric transducers have long dominated ultrasonic transducer technology, but capacitive micromachined ultrasound transducers (CMUTs) have recently emerged as an

alternative offering advantages such as wide bandwidth, ease of fabricating large arrays, and potential for integration with supporting electronic circuits. Taking this in consideration

In this context, the goal of this research work has been defined to design and fabricate a 5 meter range non-planar CMUT array for Automotive Collision avoidance. The microarray is to provide a broadband frequency independent beamforming capability without any microelectronic signal processing. Complete design specifications of the CMUT array and individual CMUTs will be carried out, a mathematical model will be developed to find the key parameters of the array, those parameters will be compared with the ones obtained using finite element analysis (FEA) method. The device was then fabricated, packaged and tested for experimental verification.

1.2   *Capacitive Micromachined Ultrasonic Transducers*

1.2.1   *Description*

A CMUT is simply a device with two plate-like electrodes biased with a DC voltage and driven with an additional AC signal to harmonically move one of the plates. The main components are the cavity, the membrane, and the electrode. Using common integrated circuit (IC) fabrication processes, a capacitor cell appears as a metallized membrane (top electrode) suspended above a heavily doped silicon substrate (bottom electrode), typical cross section of a square diaphragm CMUT is shown in Figure 1-2. An insulating layer is included to prevent the two electrodes from shorting in case of contact.
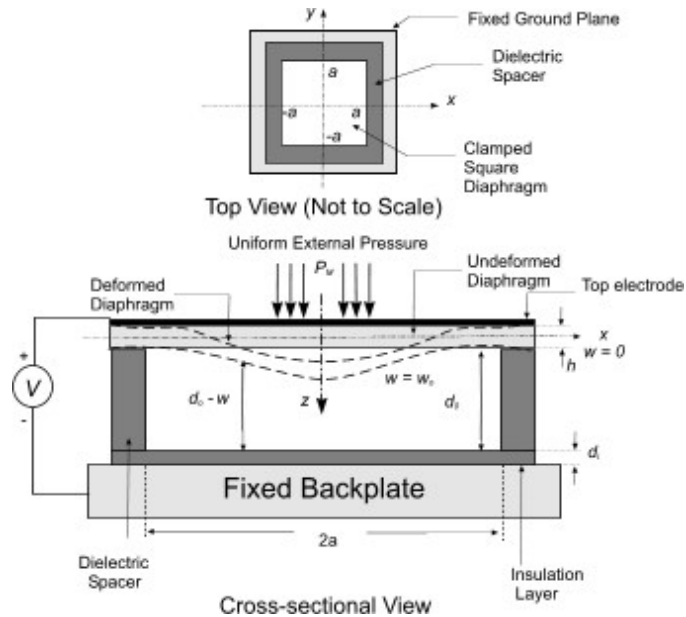
Figure 1-2 CMUT Cross Section

A single transducer element uses many small capacitor cells connected in parallel. Each CMUT

cell is a resonator with a moving membrane suspended over a cavity. The cell size and shape,

membrane topography, and configuration of insulation layers [14], can be modified to optimize

performance parameters, such as output pressure, frequency response, and reliability. A typical

CMUT geometry is built with a square, circular, or hexagonal diaphragm separated from a fixed

backplate by a small airgap.

CMUTs are operated with a dc bias voltage (Vdc) that causes the membranes to deflect

downward to a static operating point. This static operating point determines the sensitivity,

frequency response, and total acoustic output pressure. In transmit mode, an additional ac

voltage is applied to the membrane, which causes the membrane to vibrate around the static

operation point and launches pressure waves into the medium [15] [16].

CMUTs are used both as acoustic transmitters and receivers. On transmit mode, electrostatic

attraction forces are used to put the membranes into vibration by applying an AC voltage.

However, because electrostatic force is unipolar (always attraction), the vibration frequency of

10

the membranes is twice of the applied frequency. Therefore, a dc bias voltage which is larger than the ac voltage amplitude is required for proper operation of CMUTs.

The vibration of the membranes generates acoustical waves in the surrounding medium. On receive mode, harmonic vibration of the membranes, caused by an incident acoustic wave, is detected using a capacitive detection, which also requires a dc voltage. The vibrations of the membranes cause a modulation on the overall device capacitance. Under the constant bias voltage supplied, the capacitance variations result in a current flow in the external electric circuit which is amplified for further processing.

A control signal operates a switch to enable mode switching from transmit to receive and vice versa as seen in Figure 1-3. Typically, the diaphragm is created using a microfabricated thin film conductor such as aluminum or polysilicon or a composite of a non-conducting thin film structural material such as silicon nitride with a thin coating of a conducting material such as aluminum or gold on the top is used. Additionally, to avoid electrical breakdown after collapse due to the pull-in phenomenon, a thin insulation layer, either under the diaphragm conducting material or on the top of the backplate is used. Finally, a passivation layer on the top of the diaphragm is used to protect the CMUT from environmental elements [15].
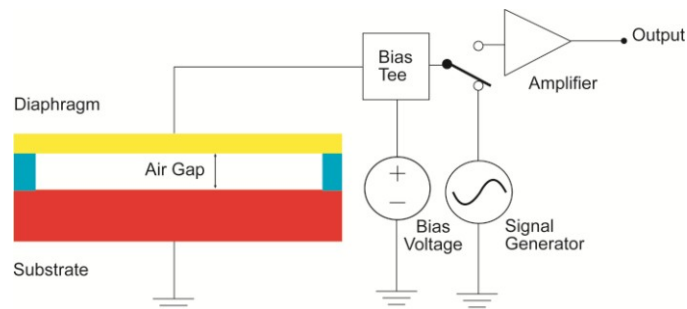
Figure 1-3 CMUT Modes of Operation

11

1.2.2   Benefits of CMUTs

Piezoelectric materials have dominated the ultrasonic transducer technology. Recently, capacitive micromachined ultrasonic transducers (CMUTs) have emerged as an alternative technology offering advantages such as wide bandwidth, ease of fabricating large arrays, and potential for integration with electronics.

Although the idea of capacitive ultrasound transducers is as old as the early piezoelectric transducers, piezoelectric materials have dominated ultrasonic transducer technology. The reason why capacitive transducers have not been popular is that electric field strengths on the order of a million volts per centimeter (106 V/cm) are required, so that electrostatic forces as large as a kilo- gram per square centimeter (kg/cm2) would be achieved, as the eminent French physicist Paul Langevin stated in 1915 [17]. However, recent advances in microfabrication technology have made it possible to build capacitive ultrasound transducers competing with piezoelectric transducers. Moreover, CMUTs offer advantages of improved bandwidth ease of fabrication of large arrays with individual electrical connections, and integration with electronics [18].

CMUT technology is not simply a low-cost replacement of piezoelectric transducer technology. Many features inherent in CMUT technology enable revolutionary advances in ultrasound technology

CMUTs provide many benefits over traditional piezoelectric transducers including improvement in performance through wide bandwidth, and ease of electronics integration, with the potential to batch fabricate very large 2D arrays with low-cost and high-yield.

The main differences between piezoelectric transducers and CMUTs can be categorized as follow:

12

Fractional Bandwidth Using piezoelectric devices in some applications is problematic due to the impedance mismatch between the piezoelectric materials and media; for example in medical applications , the characteristic impedance of piezoelectric ceramic is (≈ 33 MRayl) is significantly higher than that of various tissues like blood and fat (≈ 1.6 MRayl). For piezoelectric transducers, it makes the matching layer difficult to identify, and coupling efficiency poor. CMUTs offer better acoustic matching to the propagation medium, resulting in broader fractional bandwidth [19].

Transduction Efficiency For transducer design, one of the most important concerns is efficiency. Therefore, improved transduction efficiency, boosting both output pressure and reception sensitivity is required. For CMUTs, higher transduction efficiency can be achieved by increasing the intensity of electrical field in the CMUT vacuum cavities (high bias voltage). The dielectric layers in a CMUT can trap surface and interface charges. This trapped charges lead to major reliability issues; creates voltage drifts. Two major sources of the trapped charges are the fabrication process and the strong electrical field within the transducer cavities. Different design schemes are developed currently for CMUTs to overcome this problem (generally complicating the fabrication process) [20].

Manufacturing Conventional PZT arrays are fabricated by using "dice and fill" approach, a plate of piezoelectric material is separated by mechanical dicing and a polymer is infiltrated and cured within the kerfs. The current limit at element width is 100 μm, and 50 μm for kerf; complicated manufacturing. The fabrication process of CMUTs is based on standard silicon micromachining tehniques (or semiconductor fabrication processes).CMUTs have the ability to be integrated with the front-end electronic circuits on the same wafer. Different from piezoelectric transducers, which require a film up to more than a millimeter thick (for low frequency

application), the CMUTs are made of thin films which are typically of a thickness ranging from

from submicrometer to a few micrometers [15], [21].

The interest in CMUT research primarily arise from a number of important advantages that

CMUTs enjoy over the piezoelectric counterparts as summarized in Table 1-1

Table 1-1 Comparison of transducers technologies

	CMUT	Piezoelectric Transducer
Fabrication method	MEMS Technology	Ceramic Technology
Frequency range	Broad	Narrow
Transducer bandwidth	Wide	Moderate, matching layers required
Array Uniformity	High	Moderate
Thermal Stability	High	Low
IC Integration	Yes	No
Output Pressure	Relatively low but improving	High

1.3   Overview of MEMS fabrication technology.

Most MEMS devices and systems involve some form of lithography-bases microfabrication,
borrowed from the microelectronics industry and enhanced with specialized techniques
generally called ''micromachining''. The major techniques needed to fabricate the non-planar
CMUT array are discussed in the following sections.

1.3.1   Bulk micromachining

The oldest micromachining technology is bulk micromachining. This technique involves the selective removal of the substrate material in order to realize miniaturized mechanical components. Bulk micromachining can be accomplished using chemical or physical means, with chemical means being far more widely used in the MEMS industry.

A widely used bulk micromachining technique is chemical wet etching, which involves the immersion of a substrate into a solution of reactive chemical that will etch exposed regions of the substrate at measurable rates. Chemical wet etching is popular in MEMS because it can provide a very high etch rate and selectivity. Furthermore, the etch rates and selectivity can be modified by: altering the chemical composition of the etch solution; adjusting the etch solution temperature; modifying the dopant concentration of the substrate; and modifying which crystallographic planes of the substrate are exposed to the etchant solution.

There are two general types of chemical wet etching in bulk micromachining: isotropic wet etching and anisotropic wet etching. In isotropic wet etching, the etch rate is not dependent on the crystallographic orientation of the substrate and the etching proceeds in all directions at equal rates. In theory, lateral etching under the masking layer etches at the same rate as the etch rate in normal direction. However, in practice lateral etching is usually much slower without stirring, and consequently isotropic wet etching is almost always performed with vigorous stirring of the etchant solution, Figure 1-4 shows the isotropic etch process.

Any etching process requires a masking material to be used, with preferably a high selectivity relative to the substrate material. Common masking materials for isotropic wet silicon etching include silicon dioxide and silicon nitride. Silicon nitride has a much lower etch rate compared to silicon dioxide and therefore is more frequently used [22].

Deposit photoresist

Silicon Substrate

Patterned photoresist
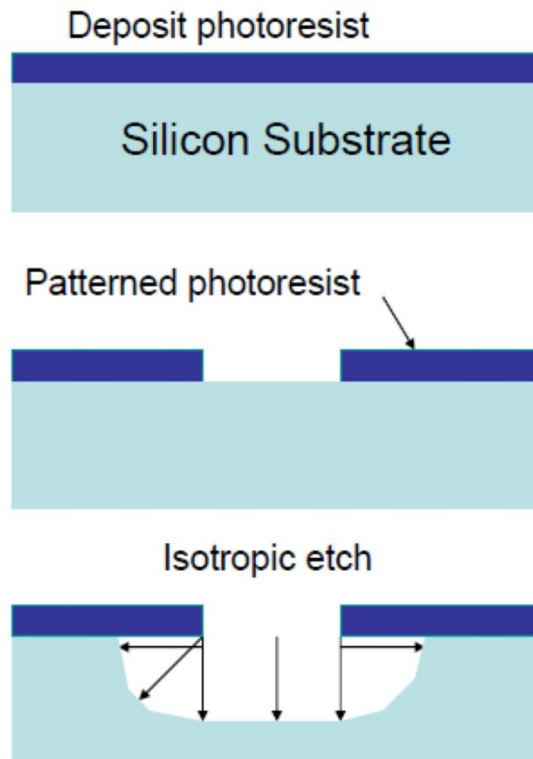
Isotropic etch

Figure 1-4 Isotropic etch process

1.3.2   Sputtering

Sputtering is a commercially important technique for thin film deposition. Sputtering is a type of physical vapor deposition and as such material is transferred directly from a source material target to the wafer. During sputtering, the source material target is charged to a high negative potential. It is then bombarded with positively charged ions from argon plasma. The target material is ejected from the source mainly by momentum transfer from neutral atoms. Ejected surface atoms are deposited onto a substrate (the wafer) placed on the anode. In order to

maximize the yield of the process, ion energies in the range of 500-3000 volts are used. Due to the large ion energies present, the deposited material is able to penetrate 1 or 2 atomic layers into the substrate, producing extremely strong adhesion [22]; Figure 1-5 shows a representation of this process.
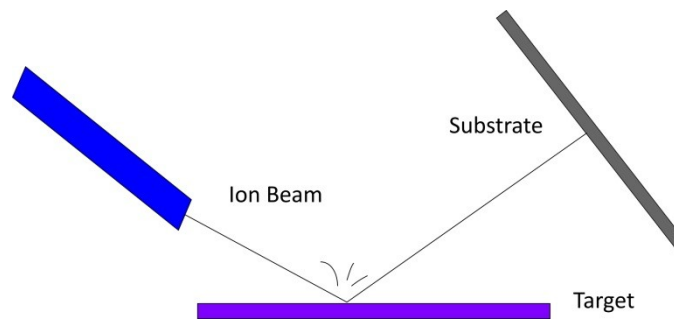
Figure 1-5 Ion Beam Sputtering

1.3.3   Spin coating

Spin coating is a technique used to apply both temporary materials such as photoresist, and permanent structural materials. Spinners are found in all microfabrication labs. The spinning process can be used to deposit viscous materials over wafers without extreme topologies. Due to poor adhesion between photoresist and metals, phosphosilicate glass (PSG) and polysilicon and polysilicon, wafers are typically 'primed' with Hexamethyl disalazane (HMDS) before the application of a photoresist. A primed wafer features a hydrophobic surface, which ensures that surface moisture on the wafer will not interfere with photoresist adhesion.

The priming process begins by baking the wafer. HMDS vapor is applied to create a monolayer on the wafer surface. An additional benefit of priming the wafers with HMDS prior to the application of a photoresist is the elimination of the effects of environmental humidity variation, Once the wafer is primed, resist is applied to the center of the wafer at approximately 300 RPM

(Figure 1-6 -A) . The spinner then rapidly accelerates to its final spin speed. This evenly spreads the resist across the wafer surface (Figure 1-6-B). Finally the spinner maintains the final spin speed for a short interval of time, typically around 1 minute (Figure 1-6-C) to allow the solvent in the resist to begin evaporating [22].
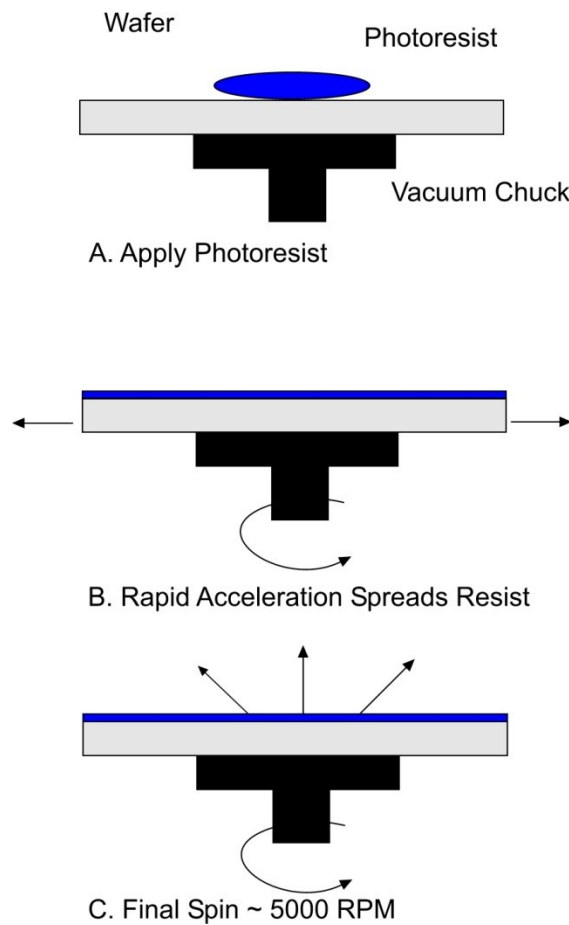
Figure 1-6 Spin Process

1.3.4 Wafer Bonding

Wafer bonding is a micromachining method that is analogous to welding in the macroscale world and involves the joining of two (or more) wafers together to create a multi-wafer stack. There are three basic types of wafer bonding including: direct or fusion bonding; field-assisted

or anodic bonding; and bonding using an intermediate layer. In general, all bonding methods require substrates that are very flat, smooth, and clean, in order for the wafer bonding to be successful and free of voids.

Direct or fusion bonding is typically used to mate two silicon wafers together or alternatively to mate one silicon wafer to another silicon wafer that has been oxidized. Direct wafer bonding can be performed on other combinations, such as bare silicon to a silicon wafer with a thin-film of silicon nitride on the surface as well.

As mentioned, wafer bonding is analogous to welding in the macroscale world. Wafer bonding is used to attach a thick layer of single crystal silicon onto another wafer. This can be extremely useful when it is desired to have a thick layer of material for applications requiring appreciable mass or in applications where the material properties of single crystal silicon are advantageous over those of thin-film Low Pressure Chemical Vapor Deposition (LPCVD) materials. Direct wafer bonding is also used to fabricate Silicon-On-Insulator (SOI) wafers having device layers several microns or more in thickness [22].

Wafer bonding was used in the fabrication of the sensor; an important fact that was considered is the need of having vacuum in the cavity, since air inside the cavity will cause ionization at a high electric field that may cause electrical breakdown to cause leakage current [23]; this point is covered with details in the Chapter 5. Wafer bonded CMUTs have been demonstrated in the literature, There are a several advantages associated with fabrication of CMUTs by wafer-bonding technology such as [24]:

- *Vacuum cavity formation*. Traditionally, the vacuum cavity is formed as follows. First, a sacrificial layer is deposited and patterned into the membrane shape. Next, the membrane that conformably covers the sacrificial layer is deposited. Later, a small hole

is etched through the membrane to access the sacrificial layer. The sacrificial layer is removed, and the membrane is released with a wet etch process. The small etch hole is subsequently sealed under vacuum to create a vacuum sealed gap between the membrane and the substrate. These steps introduce fabrication limitations to the traditional process, due to long etch times. With wafer bonding, it is easier and faster to form a vacuum cavity than it is with the surface micromachining process.

- *Cavity Size and Shape.* There are three advantages in forming the cavity with the wafer bonding technique. First, the cavity shape is independent of the membrane shape. The benefit of this is that one can separately optimize the design parameters (shape, size and height) of the cavity and membrane without any trade-off between them. Second, the aspect ratio of the cavity is no longer limited by the height of the sacrificial layer that can be deposited. Nor is it limited by the slow sacrificial layer etch. Finally, there is no unwanted material deposition onto the faces of the gap which results in a more accurate control over the gap height.

- *Membrane Size and Shape.* Since the CMUT membranes and cavities are fabricated on different wafers before bonding, the wafer bonding technique provides flexibility to design CMUTs with membranes of different size, and shape. This is due to the fact that the membrane is the active layer in the SOI wafer, which can be formed at will, independent of the cavity size and shape. All this translates into fewer limitations on the device design when trying to obtain a desired dynamic response.

- *Membrane Material.* In the wafer-bonding process, the membrane is made from single crystal silicon, which has desirable mechanical properties, e.g., few internal defects, low internal mechanical loss, and very low internal stress. This will improve the device reliability, especially important with large devices with thousands of membranes, as well

as the performance of the device. Lattice defects act as breakage nuclei while lower internal loss increases the electromechanical coupling efficiency of the device. By using an SOI wafer to form the membrane, one can achieve a good thickness uniformity (better than 2.5% of the thickness is commercially available), controllability of the stress in the membrane, and process repeatability. This is relevant with respect to commercialization of CMUT fabrication.

Despite the fact that silicon to silicon bonding has been widely used, there are some disadvantages implied in the process, being one of the most important ones the related to the high residual stress that will remain in the final product. This residual stress will affect the final behaviour of the device, modifying its specifications and compromising the reliability of the system. For that reason a new bonding process has been designed using a more reliable material, details are presented in Chapter 3 and 5.

1.4   Packaging Techniques

1.4.1   Adhesive Bonding

Adhesive bonding of a die to a package or another die may be accomplished by depositing a film of epoxy thermoset, acrylic thermoplastic or silicone resins between the layers [25]. Although the thermal and electrical conductivity of this technique are inferior to other methods of mounting, by loading the adhesive material with silver particles the electrical and thermal conductivities of the bond can be controlled over a wide range. Adhesive bonding is a low-cost technique that lends itself easily to automation. Additional cost savings can be obtained since metal plating on bonding surfaces is unnecessary. Due to the plastics used, a low curing temperature is necessary; unfortunately these plastics also need time to outgas, and are also

subject to voids. Due to the elastic properties of the bonding material, the stress in the die is reduced. The material can also be removed to allow rework of the device if necessary. Due to the nature of the bonding materials used, these devices are not suitable for use in harsh environments. Adhesive bonding is used for the non-planar CMUT array design due to the ease of integrating a large number of dies into a single package.

1.4.2   Wirebonding

Wirebonding uses thin wires to connect bond pads on the die to the packaging interconnects. The attachment process uses a combination of heat, pressure and ultrasonic energy. The result of the bonding is a weld consisting of either electron sharing or diffusion of atoms at the bond site. Pressure during the bonding ensures intimate contact between the wire and the pad, as well as helping to break up any oxide layer or contamination present at the interface. The presence of ultrasonic energy during the bond further increases the ability to break up the oxide or contaminants. The use of heat accelerates the process of atomic diffusion, reducing the amount of time necessary to form a connection [26]. The wirebonding process was used to make the connections between CMUTs in the non-planar array.

1.5   Specific Research Objectives

– To design a non-planar CMUT array for automotive collision avoidance using the theory developed in [13].

– Determine non-planar geometry suitable for fabrication using state of- the-art MEMS fabrication techniques.

– Determine sensor geometry.

– Detailed sensor design.

– Optimize the performance matrix of the sensor.

- Behaviour simulation of the sensor geometry using 3-D finite element analysis method.

- Design verification by comparing analytical results with FEA results.

- To develop a fabrication process to implement the non-planar sensor microarray.

- Fabrication and testing of the microarray.

1.6   Principle Results

The principle results of this research work have been summarized as follows:-

1. The theory developed by [13] has been used to design capacitive micromachined ultrasonic transducer based non-planar micro array. The non-planar array was designed to work at 40 kHz targeted to be used for automotive collision avoidance.

2. The design is a 5x5 array having 5 sensing surfaces along each x and y axis, with 7 different elevation levels. The array side length and height is 8.55 mm and 3.36 mm respectively. The beamwidth is 40° with maximum sidelobe intensity of -10dB.

3. A new analytical model has been developed to accurately obtain the capacitance change and load deflection profile of a square clamped diaphragm. This model incorporates the effect of biasing voltage, external pressure, fringing field and large deflections.

4. The mathematical model has been verified by comparing it with 3-D Theromoelectromechanical IntelliSuite™ based FEA to verify the results with excellent agreement.

5. A new fabrication process has been developed using for the first time BCB (Benzocyclobutene) as the isolation layer in the CMUT. A packaging process has been developed using VeroWhitePlus Fullcure835 (Plastic) to realize the non-planar structure, the non-planar array was then tested proving that the design was successful.

As a result of this work, the following paper has been published:

Journal Publication:

M. Rahman, J. Hernandez and S. Chowdhury, "An improved analytical method to design CMUTs with square diaphragms," Ultrasonics, Ferroelectrics and Frequency Control, IEEE Transactions on, vol. 60, no. 4, pp. 834, 845, April 2013.

Conference Publication:

J. Hernandez Aguirre, T. Zure and S. Chowdhury, "Capacitance Measurements of an SOI Based CMUT," in LASCAS 2013, 2013 IEEE 4th Latin American Symposium on Circuits and Systems, Cusco, 2013.

T. Zure, J. Hernandez, S. Chowdhury," Dynamic Analysis of an SOI based CMUT", Proc. Of IEEE International Conference on Industrial Technology (ICIT), 2012, 19-21 March 2012, Athens, pp. 539 - 544.

1.7   Thesis Organization

Chapter 2 deals with introducing the fundamentals of array based beamforming covered in previous work [13]. The basic theory behind and the mathematical model for designing discrete hyperbolic paraboloid is presented. The physical parameters of the array have been evaluated using the existing theory.

Chapter 3 deals with the design and simulation of the CMUT. Since the CMUTs work on the basic principle of capacitance change due to a diaphragm deflection, a novel and easy to implement mathematical model has been developed for rapid determination of the capacitance change and

diaphragm deflection profile. This model incorporates the effects of biasing voltage, fringing field capacitance, external pressure, diaphragm geometry, also accounts for the contribution of the dielectric properties of the diaphragm structural material and also the insulation layer used on the bottom electrode to prevent electrical break down and material properties. The final specifications of the sensor are presented.

Chapter 4 present the validation of the parameters of the sensor by comparing them with FEA simulations performed using Intellisuite^{TM} showing excellent agreement. A easy to implement Simulink model is presented to model the dynamic behaviour of the sensor.

Chapter 5 covers the fabrication and packaging process of the sensor, the materials used, various fabrication steps and the involved recipes are provided. The conceptual, simulation and actual photographs at various stages have also been provided. A basic set up for testing the sensor has been designed showing excellent results.

Chapter 6 makes the concluding remarks, discussions and future scope of in this specific research area.

2   CHAPTER 2

MODELING OF NON-PLANAR CMUT ARRAY

A non-planar array refers to a one or two dimensional array where the sensor elements are distributed at different elevations along the vertical axis. By constructing a non-planar array geometry a better array response over a desired frequency range will be obtained as compared to planar geometries [27]. In this chapter the theory to determine the specifications of the non-planar CMUT array for the collision avoidance application has been presented. The theory needed to design the non-planar array is presented first, and then the desired specifications for the array are presented to find the final dimensions of the array.

2.1   *Non – Planar Array Theory*

2.1.1   Beamforming

Beamforming or spatial filtering is a signal processing technique used in sensor arrays for directional signal transmission or reception [28]. This is achieved by combining elements in a phased array in such a way that signals at particular angles experience constructive interference while others experience destructive interference. Beamforming can be used at both the transmitting and receiving ends in order to achieve spatial selectivity.

It has it has been established [29] that a macroscale continuous aperture acoustical sensor having the shape of a hyperbolic paraboloid surface as shown in Figure 2-1**Error! Reference source not found.** can provide a constant beamwidth directional response without any microelectronics based signal processing.

Practically, the beamwidth should remain constant from a value governed by the physical size of the array up to the Nyquist frequency. Thus, the lateral dimensions of the array in x and y axis can be determined from the lowest operating frequency whereas the beamwidth is independently specified in each axis by the amount of out of- plane twist present at the array extremities [29].

Figure 2-1. A hyperbolic paraboloid surface

A square footprint hyperbolic paraboloid surface can be expressed in cartesian coordinate as:

$$z = y \tan\left(\frac{2\alpha x}{L}\right) \qquad (2.1)$$

Equation

$$z = y \tan\left(\frac{2\alpha x}{L}\right)$$

(2.1)

Where x , y and z are the Cartesian coordinates, L is the sidelength in x or y direction, and α is the amount of out of- plane twist in the z direction at the surface extremity (**Error! Reference ource not found.**).
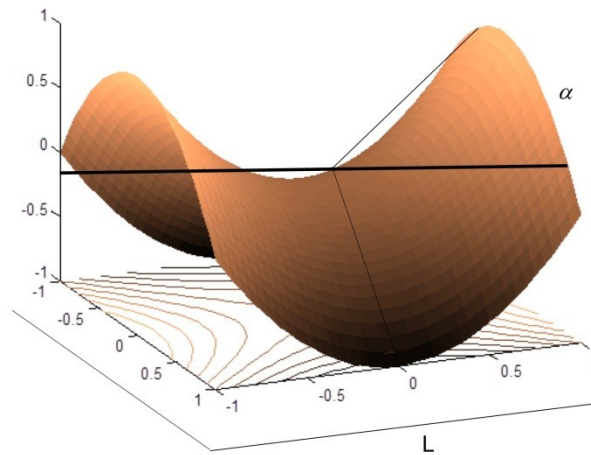
Figure 2-2 Out of plane twist angle α in a Hyperbolic Paraboloid

The far-field directional response, or array factor, of a continuous aperture hyperbolic paraboloid-shaped acoustical sensor of side length *L* in a given direction *(ϑ, φ)* as referenced from the array normal is expressed as [29]:

$$f(\theta, \phi) = \frac{1}{L^2} \int_{-\frac{L}{2}}^{\frac{L}{2}} \int_{-\frac{L}{2}}^{\frac{L}{2}} e^{j2\pi n\left(x\tan\theta + y\tan\phi + \frac{2\alpha xy}{L}\right)} \, dy dx$$

(2.4)

where:

$$n = \frac{1}{\sqrt{\tan^2 \theta + \tan^2 \phi + 1}}$$

(2.5)

Equation

(2.5) assumes that out-of-the-plane angle α is small and the sensor sidelength L is expressed in

units of wavelengths of the desired acoustical frequency.

In [29] it has been shown that the array has a reasonably constant directional response value

for large values of *1/2αL* with a small out-of-plane twist angle *α.* However, the array response

calculated   following

(2.5) is valid only if the out of the plane angle *α* is less than or equal to 10°.

The intrinsic beamforming capability of this geometry is highly desirable for use in a microarray

to minimize system power consumption and cost, while taking advantage of the scaling benefits

offered by microfabrication. Due to that the current microfabrication techniques are basically

planar processes that involve successive deposition, patterning and etching of thin films, a

continuous aperture hyperbolic paraboloid geometry transducer array cannot be fabricate using

the current microfabrication techniques. To overcome this obstacle, a discretized hyperbolic

paraboloid geometry transducer array has been suggested in the literature [13].

This discretized array can provide an intrinsic constant beamwidth beamforming capability that

can match very closely with that from a continuous aperture hyperbolic paraboloid geometry

transducer. To obtain a discretized version, the double integral in

(2.5) has been expressed as the sum of an infinite number of discrete points separated by

infinitesimal intervals using standard spatial sampling techniques, such as the Riemann

summation [30]. After performing the spatial sampling, the infinite summation can be reduced

to a finite one of an arbitrary number of levels. Out of the various Riemann Summation techniques available, center based Riemann Summation was used in this case as it is good for non-monotonic functions and its ability to calculate error bands. Following [13], the center-based Riemann summation in one dimension can be expressed as:

$$\int_a^b f(x)dx = \lim_{n\to\infty} \sum_{i=1}^n f\left(a+\left(i+\frac{1}{2}\right)\frac{b-a}{n}\right)\frac{b-a}{n} \tag{2.6}$$

Where n represents the number of discretization levels. The maximum error given for this approximation is:

$$\left|\int_a^b f(x)dx - A_{mid}\right| \le \frac{M_2(b-a)^3}{12n^2} \tag{2.7}$$

where, M_2 is the maximum value of $|f''(x)|$ and A_{mid} is the value of $f(x)$ at the midpoint of the interval a-b.

Applying $\displaystyle\int_a^b f(x)dx = \lim_{n\to\infty} \dfrac{\sum_{i=1}^n f\left(a+\left(i+\frac{1}{2}\right)\frac{b-a}{n}\right)\frac{b-a}{n}}{}$ (2.6) to

$$f(\theta,\phi) = \frac{1}{L^2} \int_{-\frac{L}{2}}^{\frac{L}{2}} \int_{-\frac{L}{2}}^{\frac{L}{2}} e^{j2\pi\left(x\tan\theta + y\tan\phi + \frac{2\alpha x y}{L}\right)} dy\,dx \tag{2.4}$$

twice, first along x axis and then along y axis, the array factor for the discretized array can be derived as [13]:

$$f(\theta,\phi) = \frac{1}{MN} \sum_{m=0}^{M-1}\sum_{n=0}^{N-1} e^{j2\pi\left((x')\tan\theta + (y')\tan\phi + \frac{2\alpha x' y'}{L}\right)} \tag{2.8}$$

Where:

$$x^{'} = \left(\frac{-L}{2} + \left(m + \frac{1}{2} \right) \frac{L}{M} \right) \ , \qquad y^{'} = \left(\frac{-L}{2} + \left(n + \frac{1}{2} \right) \frac{L}{N} \right)$$ **(2.9)**

and M and N are the number of sensing surfaces in the x and y directions respectively.

2.1.2   Array Sidelength Determination

The minimum sidelength S of the square footprint discretized hyperbolic paraboloid geometry sensor array can be determined from the following relation [13]:

$$S_{min} = \frac{Kc}{f_{lower}}$$ **(2.10)**

Where c is the speed of sound in media and f_{lower} is the lower bound frequency in the operating range. K is the fitting parameter based on the amount of acceptable beam shape variation.

As the beamwidth decreases with an increase in the frequency, empirical parameter K maintains the beamwidth within a range of $1 - 10^{\circ}$ variations for all the frequencies in a frequency range of $(f_{upper}/f_{lower}) \leq 40$. The Table 2-1 list some of the values of K for different acceptable beamwidth variation:

Table 2-1 Beamwidth Control Parameter K Values

K (Unitless)	Beamwidth variation (˚)
3	7
5	5

8	2
10	1

2.1.3   Number of Sensing Surfaces Determination

Using the following equations we can specify the number of sensing surfaces per axis for a square footprint array for -10dB and -6 dB respectively [12], [13]:

$$M, N = \left[5.69X \left(\frac{S}{\lambda_{upper}} \right)^{0.5695} - 0.8637 \right] \qquad \textbf{(2.11)}$$

$$M, N = \left[1.49X \left(\frac{S}{\lambda_{upper}} \right)^{0.9029} - 0.8484 \right] \qquad \textbf{(2.12)}$$

2.1.4   Array Height

The height of the array is directly related to the out of plane twist present at the array extremities. The maximum height measured from the center of a continuous aperture hyperbolic paraboloid geometry array can be determined from the out of plane twist angle α as $S \, tan\alpha$, where S is the sidelength of the array. The next figure shows the relation in a graphical form:
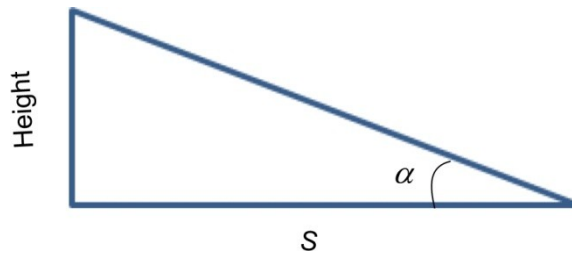
Figure 2-3 Array Height

It is known that the height has a small reduction due to the sampling point is occurring at the center of the outermost sensing surface as is shown in the Figure 2-4.
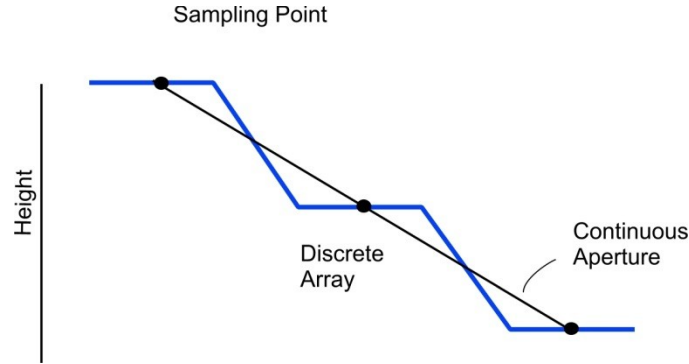
Figure 2-4 Discrete Array Height Sampling

However this sampling error introduces an angular error of less than 4.0% for arrays with more than 5 sensing surfaces per axis. This affects the beamwidth by less than $1°$ [13].

The total height for a discretized square footprint array geometry can be determined using the following equation [12]:

$$H = \left(-0.5215 \times M^{-0.792} + 0.3762\right)\frac{S\alpha}{10°}$$ (2.13)

where M represents the number of sensing surfaces in each x and y axis.

Using the theory discussed before the non-planar array was fabricated on a microfabricated tiered geometry that can approximate a discretized hyperbolic paraboloid surface as shown in Figure 2-5.
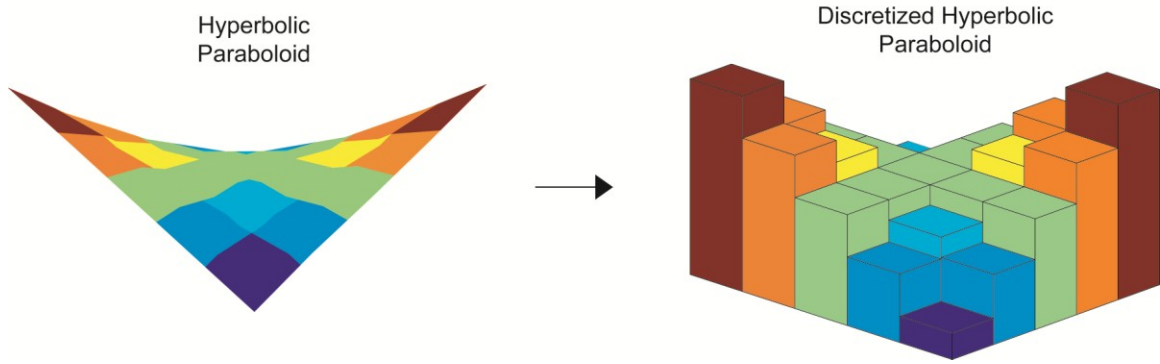
Figure 2-5 A graphical representation of the discretization process of a hyperbolic paraboloid geometry

2.2   Model Validation

It has been presented the needed theory to design a non-planar array, in order to validate it and show its scope different plots are presented. Since the wavelength of the work frequency dictate the length of the array, different beamwidth can be obtained by changing the length of the array, the following figures were plotted using a frequency of 40 KHz and changing the length of the array to show how this idea.
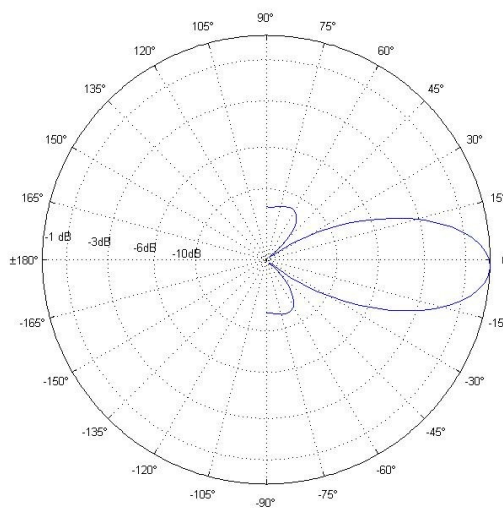
Figure 2-6 Beam shape, array length 1.6 lambda

34
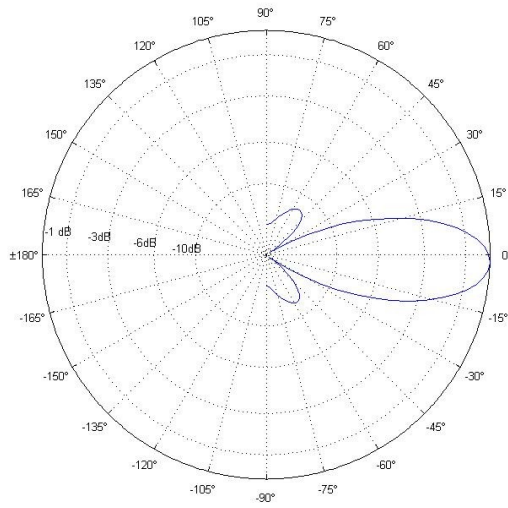
Figure 2-7 Beam shape, array length 1.8 lambda
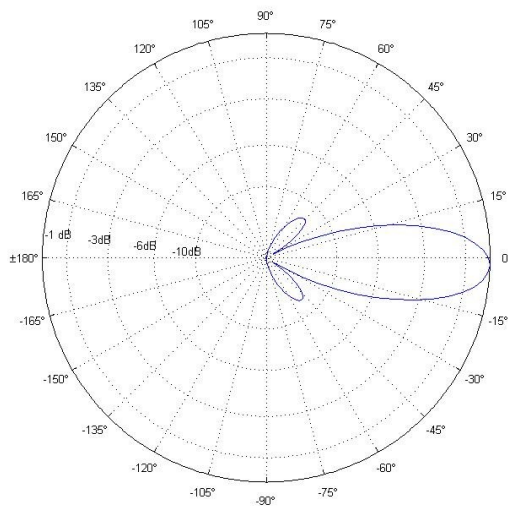
Figure 2-8 Beam shape, array length 2 lambda
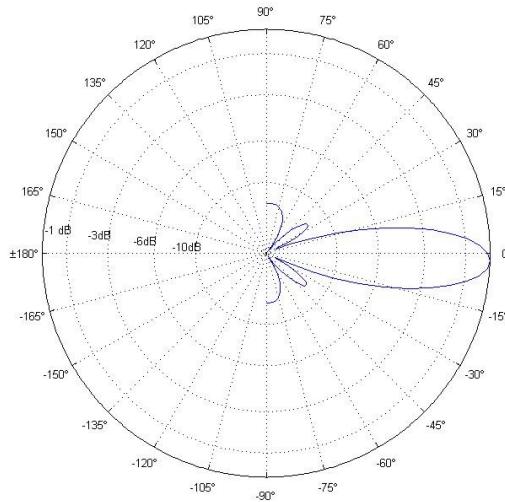
It can be seen that by changing the length of the array different beamwidth can be obtained, this point shows the flexibility of the non-planar array. It is clear that the length and height of the array is dictated by the working frequency. Shows some dimensions for different frequencies:

Table 2-2 Non-planar array dimensions for different working parameters

Frequency	Parameter	Value	Unit
40 kHz	Array length	8.57	mm
	Height	3.36	mm
	Beamwidth control parameter	1	--
113 kHz	Array Sidelength	9	mm
	Height	2.1	mm
	Beamwidth control parameter	3	--
	Array length	1.1826	mm

2.3 MHz	Height	402.1	μm
	Beamwidth control parameter	8	--

2.3   Design Methodology Non-Planar Array

In order to have ultrasound technologies and ultrasonic sensors used in automotive occupancy sensor (AOS) system such as the collision avoidance system some requirements need to be meet:

- The selected ultrasonic frequency and pressure levels should not affect humans or be heard by household pets that are likely to ride along in a vehicle equipped with an ultrasonic system.

- Natural and artificial sound sources encountered during vehicle usage should not interfere with the acoustic echo.

- Ultrasound frequencies should be chosen to minimize signal attenuation in the media and maximize reflection from the target to allow a large signal to noise ratio (SNR) enabling accurate classification.

Hearing range data for many species was evaluated as well as human exposure limits. Cats and mice have some of the highest known hearing frequencies at 91 kHz and 100 kHz respectively. Despite this fact it has been demonstrated that such animals are not disturbed by those frequencies. Ultrasonic energy guidelines are defined separately for air-coupled and contact ultrasound. For air-coupled ultrasound, the two most plausible mechanisms for non-auditory

effects are heating and cavitation. It has been reported that cavitation requires sound pressure levels (SPL) above 190 dB. Harmful effects will occur in humans for sound levels above 155 dB SPL [31].

The evaluation of frequency interference based on natural and artificial sources shows that air compressors, shotguns, sirens and keys jingling can produce high frequency interfering signals up to 120 kHz [32]. Taking those criteria into consideration the dimensions of the non-planar array will be defined.

2.3.1   Non-Planar Array Design

The array geometric design starts with the specifications of the desired operating parameters such as frequency range, beamwidth, and acceptable beamwidth variation. Once the specifications for these parameters are given, the design methodology presented in the Chapter 2 enables one to determine the necessary geometric specifications for the array in a straightforward manner. For the target application of Automotive Collision Avoidance the sensor's operating frequency will be 40 KHz since a microprocessor with this frequency will be used to excite the sensor and the maximum sidelobe intensity of less than -10dB [32], [33]. **Error! Reference source not found.** shows the final dimensions of the array and a conceptual geometry of the design is shown in Figure 2-10. The fabrication and assembly constraints have been discussed and incorporated in Chapter 5.

Table 2-3 Array Geometrical Specification

Parameter	Value	Unit
Operating Frequency	40	kHz
Beamwidth Control Parameter	1	--

Beamwidth	40˚	degrees
Array Sidelength	8.55	mm
Array Height	3.36	mm
Number of elevations	7	--
Sensing Surface per axis	5	--
Sensing Surface Sidelength	1.71	mm
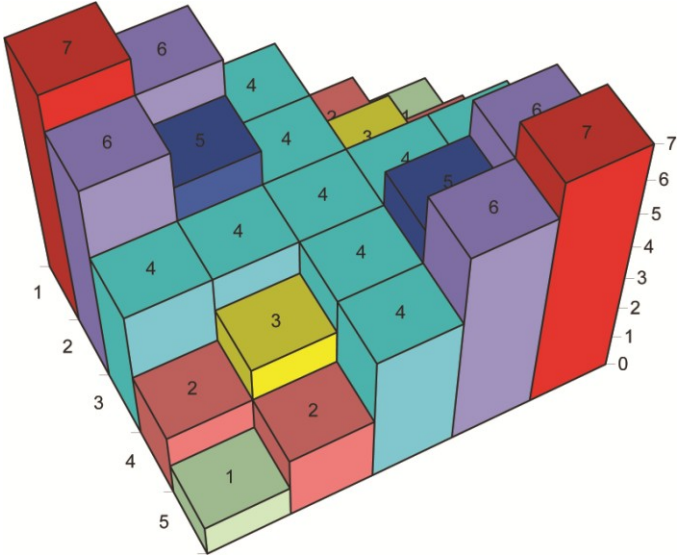
Figure 2-10 Conceptual Geometry of Non-Planar Array. Sensors having same elevation have same color

The theory and a generalized design methodology of a MEMS discretized hyperbolic paraboloid geometry ultrasonic sensor microarray have been presented. The major advantage of the developed array is that the array can provide a broadband constant beamwidth beamforming capability without any microelectronic signal processing. The developed mathematical model of discretized hyperbolic paraboloid geometry non-planar beamforming technique covers the definition of the sidelength, height, number of sensing surfaces to any desired frequency.

3   CHAPTER 3

CMUT DESIGN

This chapter cover the mathematical model and design methodology of the sensing surface of

the non-planar array. First the mathematical model to find the center deflection, deflection

shape and capacitance are presented, then the design methodology is covered in this part the

theory necessary to meet the working parameters of the sensor are developed.

Parameters like the output pressure of the sensor, working voltage, working frequency, output

current and final dimensions are presented.

3.1   *CMUT Mathematical Model*

Because the CMUT's sensing characteristics depend on the change of capacitance between the

deformed diaphragm and the backplate, accurate calculation of the capacitance between the

deformed diaphragm and the flat backplate is crucial and the calculation must take into account

1) the deformed shape of the diaphragm; 2) the contribution of the fringing field capacitance

associated with charge concentration at the diaphragm edges; and 3) the dielectric contribution

of the thin insulation layer used to protect the device against electrical breakdown. Because the

exact shape of a deformed clamped edge diaphragm is not known, generalized plate theory has

been applied by many authors to obtain a functional form of the diaphragm deformation curve that must satisfy the boundary conditions, diaphragm geometry, and the specific loading condition. The loading condition is characterized by the electrostatic loading caused by the ac and dc voltages and external ultrasonic pressure loading.

Investigation shows that more accurate analysis must include the contribution of stress and Poisson ratio mismatch between the thin films forming the multilayer laminated diaphragms. Because the boundary condition depends on specific diaphragm geometry–e.g., square, circular, or hexagonal–the load deflection model and deflection shape functions are unique for each of the cases and each demands separate treatment. Following the mathematical model to calculate the center deflection, deflection shape and capacitance of the CMUT.

3.1.1 *Center Defection of a CMUT Diaphragm*

The diaphragm center deflection determines the maximum change in capacitance for any bias voltage and electrical or ultrasonic load. In this analysis, the diaphragm is assumed to be homogeneous and isotropic with perfect edge conditions. It is assumed that the clamped edges hold the diaphragm rigidly against any out-of-plane rotation or displacement at the edges but allow displacement parallel to the diaphragm plane. At the edges, out-of-plane displacement is zero and the tangent plane to the displacement surface along the edge coincides with the initial position of the middle plane of the diaphragm. The boundary conditions imposed by the clamped edges can be expressed mathematically as [34], [35]:

$$
\left.\begin{array}{l}
w\left(x=\pm a,\ \forall y\right)=0 \\[4pt]
w\left(y=\pm a,\ \forall x\right)=0 \\[4pt]
\dfrac{dw}{dx}\left(x=\pm a,\ \forall y\right)=0 \\[4pt]
\dfrac{dw}{dy}\left(y=\pm a,\ \forall x\right)=0
\end{array}\right\}
\qquad\text{(3.1)}
$$

During the receive mode operation, the diaphragm experiences two pressure loads: an electrostatic pressure between the backplate and the diaphragm resulting from the bias voltage and the external mechanical pressure resulting from the incident acoustical waves. Following the variational method, the combined load deflection model of a clamped single-material square diaphragm subject to large deflection caused by both electrical and mechanical pressures can be expressed as [36], [37]:

$$\left[C_s f_s(v)\frac{\widetilde{E}h}{a^4}\right]w_0^3 + \left[\begin{array}{c}C_r\dfrac{\sigma_0 h}{a^2}+C_b\dfrac{12D}{a^4}\\ -\dfrac{\varepsilon_0 V^2}{2a}\left(\dfrac{2a}{d_o^3}+0.197\dfrac{a^{0.25}}{d_o^{2.25}}\right)\end{array}\right]w_0 - \left[P_M+\dfrac{\varepsilon_0 V^2}{2a}\left(\dfrac{a}{d_o^2}+0.1576\dfrac{a^{0..25}}{d_o^{1.25}}\right)\right]=0 \qquad (3.2)$$

where w_0 is the diaphragm center deflection, σ_0 is the residual stress in the diaphragm, d_o is the permittivity of free space, V is the bias voltage, D is the flexural rigidity, P_M is the external mechanical pressure, and v is the poisson's ratio of the diaphragm material. The term within the first square bracket represents diaphragm stiffness resulting from nonlinear spring hardening, the first term within the second square bracket represents diaphragm stiffness resulting from the residual stress, the second term within the second square bracket represents the diaphragm stiffness resulting from bending, the third term within the second square bracket represents electrostatic spring softening resulting from the bias voltage V, and finally, the second term within the third square bracket represents the linearized electrostatic pressure. The real root of the third-order polynomial

$$\left[C_\mathrm{s} f_\mathrm{s}(v)\frac{\widetilde{E}\,h}{a^4}\right]w_\mathrm{o}^3 + \left[\begin{array}{c}C_\mathrm{r}\dfrac{\sigma_0 h}{a^2} + C_\mathrm{b}\dfrac{12D}{a^4}\\[2mm] -\dfrac{\varepsilon_0 V^2}{2a}\left(\dfrac{2a}{d_o^3} + 0.197\dfrac{a^{0.25}}{d_o^{2.25}}\right)\end{array}\right]w_\mathrm{o}$$
$$-\left[P_\mathrm{M} + \frac{\varepsilon_0 V^2}{2a}\left(\frac{a}{d_o^2} + 0.1576\frac{a^{0.25}}{d_o^{1.25}}\right)\right] = 0 \qquad (3.2)$$

represents the center deflection of the diaphragm subject to an external pressure and the electrostatic pressure resulting from the bias voltage. Two other roots are imaginary and have no practical significance.

The constants C_r, C_b and C_s are determined by adjusting the analytical solution with the numerical results for a specific design space and following [38] their values for typical thin diaphragms are:

$$\left.\begin{array}{l}C_r = 3.45,\\ C_b = 4.06,\text{ and}\\ C_\mathrm{s} = 1.994.\end{array}\right\} \qquad \textbf{(3.3)}$$

The Poisson's-ratio-dependent function $f_\mathrm{s}(v)$ in

$$\left[C_\mathrm{s} f_\mathrm{s}(v)\frac{\widetilde{E}\,h}{a^4}\right]w_\mathrm{o}^3 + \left[\begin{array}{c}C_\mathrm{r}\dfrac{\sigma_0 h}{a^2} + C_\mathrm{b}\dfrac{12D}{a^4}\\[2mm] -\dfrac{\varepsilon_0 V^2}{2a}\left(\dfrac{2a}{d_o^3} + 0.197\dfrac{a^{0.25}}{d_o^{2.25}}\right)\end{array}\right]w_\mathrm{o}$$
$$-\left[P_\mathrm{M} + \frac{\varepsilon_0 V^2}{2a}\left(\frac{a}{d_o^2} + 0.1576\frac{a^{0.25}}{d_o^{1.25}}\right)\right] = 0 \qquad (3.2)\ \text{is}$$

given by [38]:

$$f_s(v) = \frac{1 - 0.271v}{1 - v} \qquad \textbf{(3.4)}$$

In
$$\left[C_\mathrm{s} f_\mathrm{s}(v)\frac{\widetilde{E}\,h}{a^4}\right]w_\mathrm{o}^3 + \left[\begin{array}{c}C_\mathrm{r}\dfrac{\sigma_0 h}{a^2} + C_\mathrm{b}\dfrac{12D}{a^4}\\[2mm] -\dfrac{\varepsilon_0 V^2}{2a}\left(\dfrac{2a}{d_o^3} + 0.197\dfrac{a^{0.25}}{d_o^{2.25}}\right)\end{array}\right]w_\mathrm{o}$$
$$-\left[P_\mathrm{M} + \frac{\varepsilon_0 V^2}{2a}\left(\frac{a}{d_o^2} + 0.1576\frac{a^{0.25}}{d_o^{1.25}}\right)\right] = 0 \qquad (3.2),$$

the effective Young's modulus $\widetilde{E}$ is the plate modulus and is expressed as:

$$\tilde{E} = \frac{E}{1-v^2} \tag{3.5}$$

and the flexural rigidity D is expressed as

$$D = \frac{\tilde{E}H^3}{12(1-v^2)} \tag{3.6}$$

Typical CMUT diaphragms are built with a structural material of certain thickness with a thin layer of conducting material on top of it. Load-deflection analysis of such multilayered diaphragms can be carried out using the laminar plate theory [39]. Following the laminar plate theory Eq.

$$\left[C_s f_s(v) \frac{\tilde{E}h}{a^4} \right] w_o^3 + \left[\begin{array}{c} C_r \frac{\sigma_o h}{a^2} + C_b \frac{12D}{a^4} \\ - \frac{\varepsilon_o V^2}{2a} \left(\frac{2a}{d_o^3} + 0.197 \frac{a^{0.25}}{d_o^{2.25}} \right) \end{array} \right] w_o \\ - \left[P_M + \frac{\varepsilon_o V^2}{2a} \left(\frac{a}{d_o^2} + 0.1576 \frac{a^{0.25}}{d_o^{1.25}} \right) \right] = 0$$

(3.2) can be modified to determine the load-deflection characteristics of a CMUT with multilayered square diaphragm by replacing the flexural rigidity D with the effective flexural rigidity D_{eff}, following Figure 3-1 the flexural rigidity of a multilayered diaphragm can be expressed as:

$$D_{eff} = \frac{AC - B^2}{A} \tag{3.7}$$

where the constants A, B, and C are expressed as:

$$A = \sum_k Q_k (t_k - t_{k-1}), \tag{3.8}$$

$$B = \sum_k Q_k \left(\frac{t^2_k - t^2_{k-1}}{2} \right), \tag{3.9}$$

$$C = \sum_k Q_k \left(\frac{t^3{}_k - t^3{}_{k-1}}{3} \right),$$ (3.10)

And

$$Q_k = \frac{E_k}{1 - v^2{}_k}$$ (3.11)

Where E_k and v_k are the Young's modulus and the Poisson ratio of the kth layer respectively
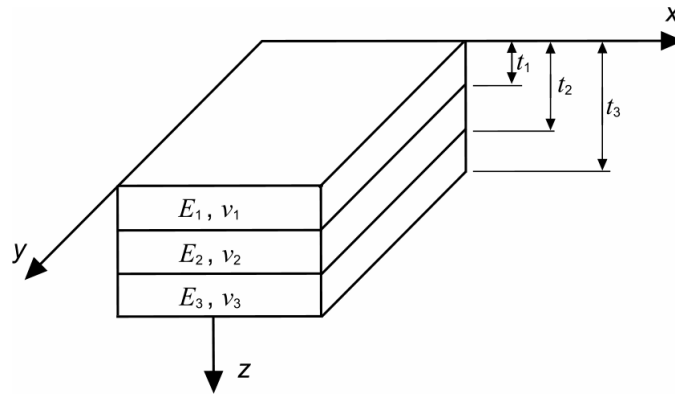
Figure 3-1 A section of a multilayered laminated plate

In order to achieve a higher accuracy in the center deflection calculation the effective airgap d_{eff} in the CMUT must be considered in the Eq.

$$\left[C_s f_s(v) \frac{\tilde{E}h}{a^4} \right] w_o^3 + \left[\begin{array}{c} C_r \frac{\sigma_o h}{a^2} + C_b \frac{12D}{a^4} \\ -\frac{\varepsilon_o V^2}{2a} \left(\frac{2a}{d_o^3} + 0.197 \frac{a^{0.25}}{d_o^{2.25}} \right) \end{array} \right] w_o \\ - \left[P_M + \frac{\varepsilon_o V^2}{2a} \left(\frac{a}{d_o^2} + 0.1576 \frac{a^{0.25}}{d_o^{1.25}} \right) \right] = 0$$ (3.2) ,

in doing so d_o will be changed by the effective airgap d_{eff} that can be calculated as:

$$d_{eff} = \frac{d_m}{\varepsilon_{rm}} + \frac{d_i}{\varepsilon_{ri}} + d_o \qquad\qquad (3.12)$$

Where d_m is the diaphragm thickness, d_i is the thickness of the insulation layer, ε_{rm} is the dielectric constant of the diaphragm structural material and ε_{ri} is the dielectric constant of the insulating layer.

3.1.2 Deflection Shape Function

Once the center deflection is obtained, deformation curve of the diaphragm can be obtained following [40]. Typical approaches to determine the deformation curve of clamped diaphragms used to design CMUTs can be grouped into 3 main categories: 1) thin plates with small deflection; 2) thin plates with large deflection; and 3) membrane approximation.

A. Thin Plates with Small Deflection ($w_0 \ll h$)

When the deflection w_0 of a thin diaphragm is very small compared with its thickness h, the transversal deformation of the diaphragm is dominated by the bending stress caused by external pressure and the residual stress developed during the fabrication process Timoshenko and Woinowsky-Krieger [35] presented an approximate mathematical expression to determine the deformation curve for thin plates in the small deflection regime using a trigonometric series. However, the model is computationally expensive because it requires extensive numerical calculations to determine a set of coefficients.

B. Thin Plates With Large Deflection

When the deflection w of a thin diaphragm becomes comparable to or larger than its thickness, the strain energy resulting from stretching of the middle plane of the diaphragm can no longer

be ignored. For this case, stretching of the diaphragm mid-plane along with the bending stress and the residual stress developed during the fabrication process must be taken into consideration. Functional forms based on polynomials using the Rayleigh‑Ritz energy method [41] and sine/cosine functions in the form of Fourier series using von Karman equations [42] have been explored by many authors. However, these methods are computationally very expensive and an exact solution would require infinite number of terms.

C. Membrane Approximation

Timoshenko and Woinowsky-Krieger [35]and Maier- Schneider et al. [38] used a membrane approximation method to determine the center deflection and the deformation curve for clamped thin diaphragms. For a thin membrane that has much larger lateral dimensions than its thickness, strain energy resulting from bending becomes negligibly small compared with those resulting from the residual stress and nonlinear stretching of the middle plane. As the bending moment at the clamped edge is zero, unlike the plates, zero gradient of the tangent plane to the displacement surface along the edge is no longer a required boundary condition for membranes [35], [38]. Timoshenko and Woinowsky-Krieger [35] proposed a membrane deflection shape function based on a double cosine approach which is a one-term approximation of a Fourier series that represents the deflection shape. Following this approach, the membrane deformation curve along either the x or y axis mimics the single-mode vibration of a string fixed at both ends where the displacements normal to the initial string position at the fixed nodes are zero but the tangents to the string at the nodes are not zero. However, the model fails to describe the diaphragm's real bending shape accurately and the authors in [38] improved the accuracy of the model by adding two empirical terms to minimize the deviation from FEA and experimental results. Though the modified model shows excellent agreement with experimental

results for thin diaphragms with relatively large side lengths, it has been shown that that it does not agree well with the deflection shapes of thicker diaphragms that behave more like plates [40].

The new deflection shape function has been developed by modifying the equations presented in [35] for thin plates in large deflection while considering the effective flexural rigidity D_{eff} for a multilayered composite diaphragm. Following [35], the lateral and transverse displacements of a rigidly clamped thin plate with side lengths $2a$ and $2b$ can be approximated by:

$$
\begin{aligned}
u &= \left(a^2 - x^2\right)\left(b^2 - y^2\right)x\left(b_{00} + b_{02}y^2 + b_{20}x^2 + b_{22}x^2y^2\right) \\
v &= \left(a^2 - x^2\right)\left(b^2 - y^2\right)y\left(c_{00} + c_{02}y^2 + c_{20}x^2 + c_{22}x^2y^2\right) \\
w &= \left(a^2 - x^2\right)^2\left(b^2 - y^2\right)^2\left(a_{00} + a_{02}y^2 + a_{20}x^2\right)
\end{aligned}
\tag{3.13}
$$

Where u and v are the displacements in the middle plane of the plate along x and y directions, respectively, and vanish at the boundary and w represents the transverse deflection. As w also vanishes at the boundary and so does its first derivative, all the necessary boundary conditions imposed by the clamped edges are satisfied by **Error! Reference source not ound.**). The undetermined parameters $b_{00}, ..., a_{20}$ in **Error! Reference source not found.**) can be determined by applying the principle of virtual displacement and an energy minimization method [35]. However, determination of eleven undetermined parameters is computationally quite expensive as it will involve numerical solutions of eleven simultaneous non-linear equations using the method of successive approximation. Most notable feature of **Error! eference source not found.**) is that the polynomial basis function $\left(a^2 - x^2\right)^2\left(b^2 - y^2\right)^2$ captures the actual shape of the deformation curve with an accuracy higher than the double cosine

squared [34] or double sine squared [43] functions and the quantity a_{00} is associated with the center deflection of the diaphragm that can be calculated following (3.2) with the modification for D_{eff} as shown in **Error! Reference source not found.**). Instead of trying to determine eleven undetermined parameters by solving eleven simultaneous non-linear equations using the method of successive approximation each time, a simple and straightforward approach can be to formulate a deflection shape function with the same basis function as in **Error! Reference source not found.**) and then determine one or two empirical parameters that capture the contribution of eleven unknown parameter values with reasonable accuracy for a target design space. Following this approach, a trial deflection shape function as shown in (3.14) has been formulated:

$$w = w_0 \left(1 - \frac{x^2}{a^2} \right)^2 \left(1 - \frac{y^2}{a^2} \right)^2 \left[1 + c_1 \left(\frac{x^2 + y^2}{a^2} \right) + c_2 \left(\frac{x^2 + y^2}{a^2} \right)^2 \right]$$
(3.14)

Where the term associated with the coefficient c_1 adjusts the deflection profile for the center region $(0 < x < 0.5a)$ and the term associated with the coefficient c_2 adjusts the deflection profile for the outer region $(x > 0.5a)$ of the diaphragm to match with FEA results. The above equation can be re-written in a general form as:

$$w = w_0 \left(1 - \frac{x^2}{a^2} \right)^2 \left(1 - \frac{y^2}{a^2} \right)^2 \sum_{n=0,1,2}^{N} c_n \left(\frac{x^2 + y^2}{a^2} \right)^n$$
(3.15)

where the coefficients c_n are adjustable for any design space and are to be determined from FEA simulation results. For a CMUT with a diaphragm thickness range of 0.5-3 μm and sidelength range of 200-1000 μm, investigation shows that three terms $(N = 2)$ in (3.15) are necessary for large deflection cases while only two terms $(N = 1)$ are necessary for small

deflection cases to achieve a high degree of accuracy. For the specified design space, the parameters c_o, c_1, and c_2 are determined as [40]:

$$\left. \begin{array}{l} c_0 = 1 \\ c_1 = \dfrac{0.0011}{\sqrt{h}} \\ c_2 = \dfrac{0.0005}{\sqrt{h}} \end{array} \right\}$$

(3.16)

3.1.3 Capacitance

Because the diaphragm lies in the *x–y* plane, the parallel plate capacitance between the deformed diaphragm and the backplate can be calculated following [44]:

$$C_{\text{Deform}} = \varepsilon_0 \iint_A \frac{dxdy}{\dfrac{d_m}{\varepsilon_{rm}} + \dfrac{d_i}{\varepsilon_{ri}} + d_o - w(x,y)}$$

(3.17)

Where $w(x,y)$ is the deflection shape function that provides the deflection profile of the deformed diaphragm given by Eq. (3.15). Commonly used parallel plate capacitance model as expressed in (3.17) does not take account of the fringing field effects that is associated with the electric flux lines originating from diaphragm sides and charge concentration at the diaphragm edges. It has been shown [40] that for small diaphragms used in typical CMUTs, the contribution of fringing field capacitance can be as high as 9% of the parallel plate capacitance. Though an accurate value of the fringing field capacitance can only be obtained by solving Poisson's equation using a 3-D field solver, a highly accurate value of the fringing field capacitance can be calculated by modifying a VLSI on-chip interconnect capacitance model presented in [36].
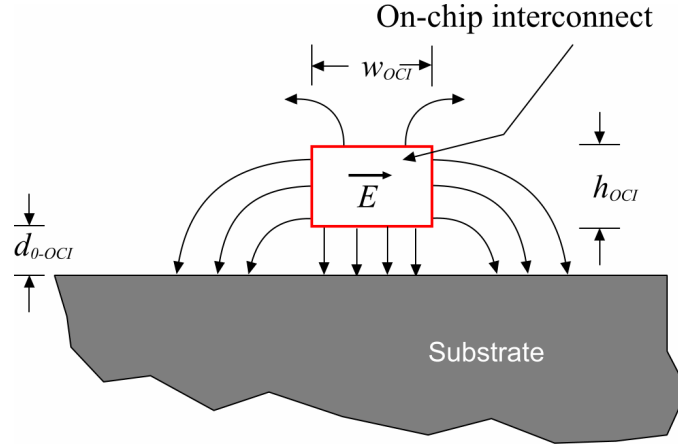
On-chip interconnect

Following [36]the per unit length capacitance of a VLSI on-chip interconnect of width w_{OCI} and

thickness h_{OCI}, separated from the substrate by a dielectric medium of thickness d_{0-OCI} and

relative dielectric constant ε_r, as shown in Figure 3-2 can be expressed as:

$$C_{OCI} = \varepsilon_0 \varepsilon_r \left[\left(\frac{w_{OCI}}{d_{0-OCI}} \right) + 0.77 + 1.06 \left(\frac{w_{OCI}}{d_{0-OCI}} \right)^{0.25} + 1.06 \left(\frac{h_{OCI}}{d_{0-OCI}} \right)^{0.5} \right] \qquad \textbf{(3.18)}$$

It has been determined that the maximum deviation of (3.18) from the most accurate numerical

method presented in [36] is only 2% when $w_{OCI} / d_{0-OCI} \geq 1, \ 0.1 \leq h_{OCI}/d_{0-OCI} \leq 4$ and 6% as

long as $w_{OCI}/d_{0-OCI} \geq 0.3, h_{OCI}/d_{0-OCI} \leq 10$ holds. An approximate value of the fringing

field capacitance for a CMUT fabricated with a square diaphragm of sidelength $2a$ as shown in

Figure 1-2 can be calculated by modifying **Error! Reference source not found.** as:

$$C = \frac{4\varepsilon a^2}{d_{eff}} + 1.44\varepsilon a + 2.12\varepsilon a \left(\frac{2a}{d_{eff}} \right)^{0.25} + 2.12\varepsilon a \left(\frac{d_c}{d_{eff}} \right)^{0.5} \qquad \textbf{(3.19)}$$

The first term in (3.19) represents the parallel plate capacitance associated with the CMUT. The

second and third term together represent the fringing field capacitance due to the diaphragm

sidelength $2a$ while the fourth term represents the fringing field capacitance due to the conductor thickness d_c. By rearranging (3.19) a functional form of total capacitance associated with a CMUT can be derived as:

$$C = C_o (1 + C_{\text{ff}})$$

(3.20)

Where C_0 is the parallel plate capacitance expressed as:

$$C_0 = \frac{\varepsilon_0 4a^2}{d_{\text{eff}}}$$

(3.21)

and C_{ff} is the fringing field factor expressed as:

$$C_{\text{ff}} = \frac{0.385}{a} \left[d_{\text{eff}} \right] + 1.06 \left[\frac{1}{2a} \{ d_{\text{eff}} \} \right]^{0.75} + \frac{0.53}{a} \left[d_c \{ d_{\text{eff}} \} \right]^{0.5}$$

(3.22)

The third term in (3.22) represents the fringing field capacitance due to the conductor thickness d_c and can be neglected as the flux lines originating from the conductor sides along the thickness will terminate beyond the coupling area of the device and will not contribute to the total capacitance.

After deformation, the total capacitance is also contributed by two factors: the parallel plate capacitance C_{Deform} between the deformed diaphragm and the backplate which can be calculated using (3.17), and the fringing field factor C_{ff}. Thus the total capacitance after deformation can be expressed as:

$$C = C_{\text{Deform}} (1 + C_{\text{ff}})$$

(3.23)

As the diaphragm edges are rigidly fixed and don't undergo any deformation and as the fringing field capacitance is contributed mainly by the charges concentrated at the edges, the fringing

field factor C_{ff} can be assumed to remain unchanged despite diaphragm deformation and (3.22) can be used to calculate C_{ff} as before.

3.2   *Design Methodology Sensing Surface*

For transducers to excite and detect efficiently ultrasound in the coupling medium there must be a good acoustic impedance matching between the transducer and coupling medium itself. Currently, commercial ultrasound transducers are piezoelectric devices, but their acoustic impedance is much larger than that of air and, as a consequence, transmission losses occur at the interface between the transducer and the coupling medium. In order to reduce this problem, matching layers can be placed between the piezoelectric device and the gas medium, resulting in better acoustic impedance coupling [45]. Micromachined 1‑3 connectivity piezocomposites are also being investigated for matching piezoelectrics into air [46]. Nevertheless, the manufacture complexity of these technologies increases the cost and reduces the device reliability.

CMUTs, on the contrary, are able to generate ultrasound efficiently in air, as their thin membranes match well the acoustic impedance of air [47]. This results in large dynamic range, enabling air applications, as air-coupled non-destructive testing.

Long-distance and short-distance ranging transducers can be manufactured by CMUT technology, varying the size of the thin membranes suspended over the substrates and then their resonance frequency, and exploiting the CMUT's high dynamic range that allows operating at high frequency and measure large distance (detection of ultrasound reflection up to 10 meters despite high attenuation in air). Taking this in consideration a model to find the required

output pressure coming from the non-planar array is necessary and to define working voltage, resonant frequency and capacitance change in the CMUT sensor while working become primordial, in order to obtain that a parallel-plate capacitor model for CMUT must be explored.

3.2.1   Parallel-plate Capacitor Model for CMUT

When actuated by an electrostatic or a mechanical force, a CMUT membrane deflects and therefore exerts a restoring force. This can be modeled using an equivalent spring. The energy loss mechanisms in a CMUT, including the loss within CMUT structure and the energy coupling into the medium, can be lumped into a dissipative damping element. Thus, a parallel-plate capacitor model that consists of spring-mass-dashpot is suitable for analyzing the CMUT structure Figure 3-3.
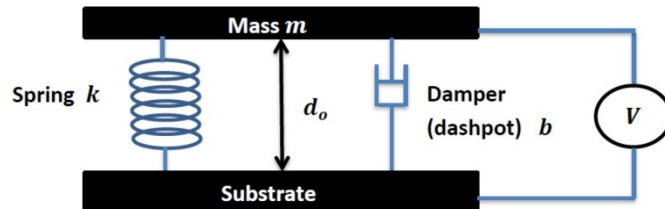
Figure 3-3 Parallel-plate capacitor model for CMUTs

In this model, the membrane is simplified as a rigid plate with an equivalent mass m supported by a spring with an equivalent spring constant k anchored on a substrate. A damping factor b is used to represent all mechanical and acoustical damping mechanisms in the CMUT. V represents the voltage that is applied between the membrane and substrate. The mass and the substrate are also the top and bottom electrodes of the CMUT in the model, respectively. The substrate is fixed mechanically; d_o represents the distance between the membrane and the substrate, which is also the spring length. Newton's Second Law dictates that the equation for

54

the membrane displacement x, which is defined as $w_o - d_o$ (where d_o is the initial gap height), is:

$$m\ddot{x} = m\ddot{g} = \sum F = F_e + F_m + F_s + F_b,$$ (3.24)

Where F_e represents the electrostatic force applied on the membrane. F_e is a function of the applied voltage and the distance d_o [15]:

$$F_e = -\frac{\varepsilon_o A V^2}{2d_o}$$ (3.25)

Where A is the equivalent area of the capacitor structure of the CMUT. F_m represents the acoustic or mechanical force applied by the medium. F_s represents the spring restoring force, which is also a function of the distance d_o:

$$F_s = -k(d_o - w_o) = -kx$$ (3.26)

The last term F_b represents the damping force, which includes all mechanical and acoustical losses of the CMUT membrane. It can be expressed as:

$$F_b = -b\dot{d}_o = -b\dot{x} = -bv = -(b_m + Z_m)v,$$ (3.27)

Where b_m and Z_m represent the loss factor within the transducer and its packaging structure, and the acoustic loss factor to the medium, respectively. The acoustic loss factor Z_m (loading impedance of the medium on the transducer) represents the efficiency of power delivery from a CMUT to the medium, and is therefore an important parameter. Usually, Z_m is a complex entity so it affects not only the bandwidth of the CMUT, but also the center frequency.

3.2.2 Output Pressure Transmitted

In transmission, the input is an electrical actuation voltage, and the output is an acoustic wave delivered to the medium through the membrane of the CMUT. Equation (3.24) can be written as:

$$\sum F = F_e + F_m + F_s + F_b = m\ddot{x}, \qquad (3.28)$$

and $F_e = m\ddot{x} + b\dot{x} + kx,$ (3.29)

The actuation AC signal $V_{ac}(t)$ applied on the CMUT introduces an electrostatic force. An optional DC voltage V_{dc} may be added on the AC signal to set the static operation point. The total electrostatic force can be written as:

$$-F_e = -\frac{\varepsilon_o E^2 A}{2} = \frac{\varepsilon_o A}{2d_o^2}\left(V_{dc}^2 + V_{ac}(t)^2 + 2V_{dc}V_{ac}(t)\right) \qquad (3.30)$$

Thus, equation (3.29) can be written as:

$$\frac{\varepsilon_o A}{2d_o^2}\left(V_{dc}^2 + V_{ac}(t)^2 + 2V_{dc}V_{ac}(t)\right) = m\ddot{x} + b\dot{x} + kx \qquad (3.31)$$

In equation (3.31) $V_{ac}(t)^2$ can be decomposed into a second harmonic term and a DC term. The resulting DC terms set the DC operation point. The second harmonic term can be ignored for analysis at the fundamental frequency. The differential equation can be written as:

$$m\ddot{x} + b\dot{x} + kx = \frac{\varepsilon_o A V_{dc} V_{ac}(t)}{d_o^2} = CEV_{ac}(t), \qquad (3.32)$$

Where $C\left(C = \varepsilon_o A / d_o\right)$ and $E\left(E = V_{dc} / d_o\right)$ are the capacitance of the CMUT capacitor structure and the electrical field strength in the gap between the two electrodes. Unfortunately, there is no analytical solution for this simplified equation because d_o, C and E are all functions of time. However, Equation (3.32) shows that CMUTs with a larger capacitance and stronger electric field (i.e. a small gap g and larger bias voltage V_{dc}) have better coupling efficiency between the electrical and acoustic domains in transmission.

This fact gave us the mathematical foundation to design a CMUT with a small gap and a large bias voltage.

A essential parameter of the CMUT is the maximum output pressure. The output pressure is given by:

$$P_a = \mathrm{Re}(Z_m v),$$ \hfill **(3.33)**

For an output acoustic wave with frequency ω, the pressure is:

$$P_a = \mathrm{Re}(Z_m v) = \mathrm{Re}(Z_m)\omega A_a,$$ \hfill **(3.34)**

Where ω is the angular frequency , A_a is the displacement due to the electrostatic pressure caused by the V_{ac} voltage applied to the membrane, and $\mathrm{Re}(Z_m)$ is the real part of the medium loading impedance, since the sensor will be operating in air, the impedance is a real value and is equal to 413 Rayls. At a certain operation frequency, the output pressure is directly proportional to the equivalent piston-shape displacement of the membrane. This is analogous to the Ohm's Law in electrical circuits: the electrical voltage (analogous to acoustic pressure) across a load resistor (analogous to acoustic medium) is proportional to the electrical current

(analogous to membrane velocity which is given in part by the frequency of the V_{ac} applied to the CMUT).

The maximum displacement of the CMUT membrane, hence the maximum output pressure, is limited by the gap between the two electrodes. Moreover, the pull-in effect of a parallel-plate capacitor may further limit membrane displacement. As a result a large electrode gap is desirable for higher output pressure. However, a small gap is needed for better transduction efficiency (Equation (**3.32**). Therefore, there is a trade-off in setting the electrode gap d_o in the CMUT design.

Using the center deflection due to the V_{ac} applied to the CMUT from equation

$$\left[C_s f_s(\nu) \frac{\widetilde{E} h}{a^4} \right] w_o^3 + \left[\begin{matrix} C_r \frac{\sigma_0 h}{a^2} + C_b \frac{12D}{a^4} \\ - \frac{\varepsilon_0 V^2}{2a} \left(\frac{2a}{d_o^3} + 0.197 \frac{a^{0.25}}{d_o^{2.25}} \right) \end{matrix} \right] w_o$$
$$- \left[P_M + \frac{\varepsilon_0 V^2}{2a} \left(\frac{a}{d_o^2} + 0.1576 \frac{a^{0.25}}{d_o^{1.25}} \right) \right] = 0$$

(**3.2**) as

$\left(A_a \right)$ in the equation (3.34) and the air impedance (413 Rayls) we can find the output pressure generated by the CMUT with a given frequency in the V_{ac} signal.

After determination of the array geometric specifications and the establishment of the model to find the output pressure of the sensor, transducer level modeling is done to obtain the geometry of individual capacitive sensors and optimize the performance of the sensor.

3.2.3   Resonant Frequency

The center frequency of a system as the one presented in the Figure 3-3 is determined by the natural resonant frequency of the membrane and the complex damping factor b. The natural resonant frequency of the membrane is determined by the equivalent mass m and the spring k as $w_o \sqrt{k/m}$. In general, there is no analytic formula to calculate the resonant frequency of a

membrane. It is usually simulated using finite element methods. In some special cases there exist analytical formulae for the resonant frequency. Following [48] the resonant frequency of a CMUT can be found using:

$$f_{res} = \sqrt{\frac{1}{\rho}\left(\frac{D_{eff}\pi^2}{a^4} + \frac{T}{2a^2}\right)}$$

(3.35)

where D_{eff} is the effective flexural rigidity, a is half the sidelength of the membrane, ρ is mass per unit area of the diaphragm and T is tensile force per unit length which is calculated as:

$$T = h\sigma$$

(3.36)

where σ is the residual stress of the diaphragm.

3.2.4   Pull-in and Working Voltage

Similar to any parallel-plate electrostatic capacitor structure, a pull-in (collapse) voltage exists for the CMUT membrane. Pull-in occurs when the electrostatic force overcomes the mechanical restoring force, and the membrane abruptly snaps down to the substrate. Usually a CMUT is designed to operate at a bias voltage less than the pull-in voltage [22]. However, a CMUT can also be operated beyond pull-in point to achieve a higher center frequency and enhanced transduction efficiency and fractional bandwidth. Determining the pull-in voltage is critical in the design process in order to determine the optimum DC operating point of the CMUT as increasing the DC bias voltage increases the sensitivity of the device. The pull-in voltage for a square diaphragm CMUT as shown in can be calculated following:

$$V_{pi} = \sqrt{\frac{\left(\dfrac{C_r \sigma h}{a^2} + \dfrac{C_b 12 D_{eff}}{a^4}\right) + \left(\dfrac{C_s f_s(v)\tilde{E}h}{a^4}\right)\dfrac{d_{eff}^3}{9}}{3\varepsilon_0 \left(\dfrac{0.665}{d_{eff}^2} + \dfrac{0.2231 a^{-0.75}}{d_{eff}^{1.25}}\right)}}$$

(3.37)

Since the sensor will be working in an automobile the pull-in voltage must be bigger than the 12 volts used as the bias voltage.

3.2.5   Receive Sensitivity

During receive, the input of the CMUT is acoustic pressure (force) F_m from medium and the output is the capacitance change of the CMUT. Equation (3.24) can be written as:

$$\sum F = F_e + F_m + F_s + F_b = m\ddot{g} = m\ddot{x},$$

(3.38)

The electrostatic force is introduced by a bias voltage V_{dc}. The bias voltage applied on the CMUT also converts the capacitance change into electric current, which is detected by the front-end circuit of the CMUT. The electrostatic force can be written as:

$$-F_e = -\frac{CV_{dc}^2}{2d_o} = \frac{\varepsilon_o A V_{dc}^2}{2d_o^2};$$

(3.39)

During reception, the displacement of the CMUT membrane is much smaller than the gap d_o. The displacement of the membrane results in a capacitance change that is measured by monitoring the current under a constant bias voltage. The amplitude of this current output is a function of the frequency of the incident wave, the bias voltage and the capacitance of the device. The magnitude of the current resulting from n parallel membranes can be expressed as [49]:

60

$$I = 2\pi f V_{dc} nC \frac{\Delta x}{d_o} \qquad\qquad \textbf{(3.40)}$$

Where f is the ultrasound frequency, V_{dc} is the bias voltage, C is the capacitance of a single membrane, d_o is the separation between the electrode and the substrate, and Δx is the magnitude of the displacement. The resulting current is then amplified with a transimpedance amplifier.

To increase the displacement sensitivity of a CMUT as an ultrasonic detector, there are three parameters to optimize.

We can increase the bias voltage, which is limited by the collapse voltage. We can decrease the gap between the membrane and the substrate. But, this is not as effective as it seems because decreasing the gap decreases the collapse voltage as well. Finally, we can increase the total capacitance by increasing the number of membranes (n) and/or the area of the individual membrane.

3.3   Final Design Specifications

Following the mathematical models and design methodology presented above, a CMUT has been designed and analytically analyzed using Matlab™. Important working facts need to be considered to decide the final specifications such as:

- The sensor will be used in an automobile which means that in order to reduce the complexity of the system a bias voltage of 12 V needs to be used to set the operation point of the sensor.

- The ultrasonic beam coming from the sensor will be traveling a total distance of 10 meters, 5 meters to reach the target and the 5 meters that the echo signal will travel to return to the sensor.

- The beam has to have enough power to go about the 5 meters, crash the target and return to the sensor traveling the 5 meters again.

- The bias voltage must be away from the pull-in voltage to ensure proper operation.

- The working frequency of the sensor will be 40 kHz since this will be the frequency of the signal applied from the microprocessor, so the resonant frequency of the sensor must be bigger than this value to ensure proper operation.

Previous works gave us insight of some proper dimensions for the design of the CMUT with those characteristics [50], [51], an important fact to consider in the definition of the dimensions of the CMUT's is the total number of CMUT's that can be located in each tier of the non-planar array, this number will define the output pressure coming from the sensor and the output current that the sensor will generate with the echo signal. Final design specifications of the CMUT are summarized in Table 3-1 Final CMUT Design Specification.

Table 3-1 Final CMUT Design Specification

Parameter	Value	Unit
Operating Frequency	40	kHz
Bias Voltage	12	V_{DC}
Resonant Frequency	10.08	MHz
Pull-in voltage	951	V_{DC}
AC voltage applied	18	V_{AC}
Airgap	1.1	µm
Diaphragm thickness	0.8	µm

Diaphragm Sidelength	28	μm
Output Pressure generated by CMUT	0.0241	Pa

Based in previous work [51] silicon has been chose as diaphragm material, is reliable and its mechanical characteristics are well known and is easy to implement in a SOI (Silicon on insulator) based process. However silicon to silicon bonding generates some difficulties in the final design, one of the most important of these issues is the related to the high residual stress that will remain in the final device and will affect its final behaviour. Considering this a different material has been chose to perform the bonding process, this material is BCB (Benzocyclobutene).

BCB has many figures of merit such as low dielectric constant, a low electrical current loss factor at high frequencies, low moisture absorption, low cure temperature, high degree of planarization, and low level of ionic contaminants, high optical clarity, good thermal stability, excellent chemical resistance, and good compatibility with various metallization systems [52]. Lower ionic contamination prevents leakage currents and charge traps, this point in particular is of high relevance since in previous designs those charges have been the responsible of discrepancy between measurement [23], this point is covered in chapter 5.

Once the dimensions of the CMUT are defined we can determined the amount of CMUT's to be placed in each tier and from then to calculate the total output pressure of the sensor and the total current resulting from the echo signal.

Following the relation (3.40) it's clear that the more CMUT's are connected in parallel the more the output current that will be generated from the sensor with the echo signal. Considering that the total length of the array is 8.55 mm and that will be 5 sensing surface per side then each of

those sensing surface will have a length of 1.71 mm and since the sidelength of each CMUT is 28 μm a total number of 40 CMUTs can be placed per side. Figure 3-4 shows the layout of a single tier, discussion about the reason of the final dimensions of the sensor will be presented in Chapter 5.
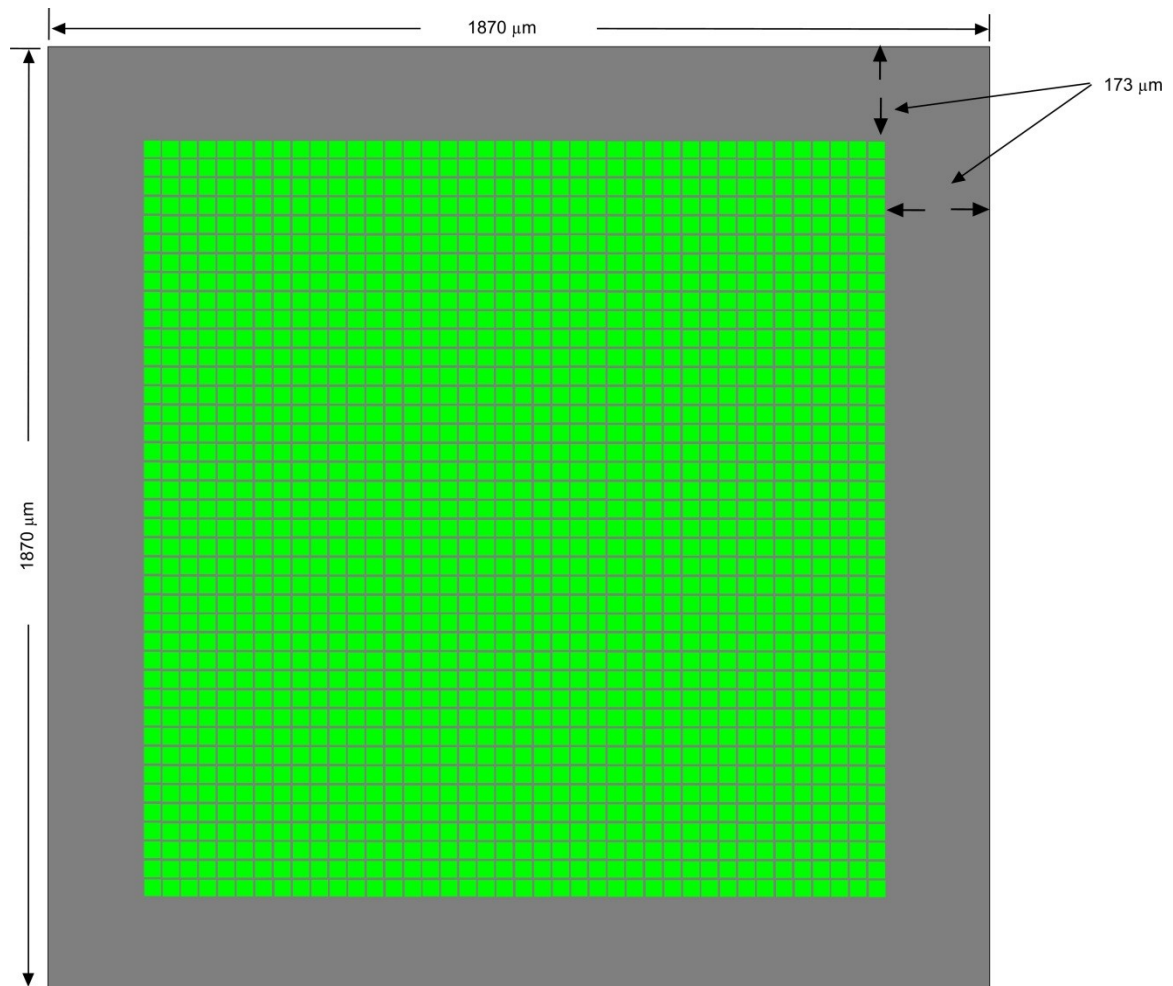

Figure 3-4 Single Tier Layout

Since airborne ultrasound is usually quantified in terms of sound pressure level (SPL) in decibels (dB), is necessary to convert the output pressure from Pa to dB this is done using the following formula [53]:

(3.41)

$$SPL(dB) = 20\log_{10}(p/p_r),$$

Where p is the root mean square acoustic pressure and p_r is the reference pressure. p_r is equivalent to approximately the lowest level of audible sound perceived by humans at the most sensitive frequency, and is normally taken as equal to 20 micropascals (μPa).

Since all the CMUTs have the same dimensions and will be excited with the same voltage they will generate the same amount of output pressure so the CMUTs can be treated as equal sound power sources, considering this the total output pressure coming from the sensor can be calculated using [54]:

$$L_{pt} = L_{ps} + 20\log(n), \qquad\qquad\qquad\qquad \textbf{(3.42)}$$

Where L_{ps} is equal to the pressure generated by one pressure source (dB re 20 μPa RMS), n is the total number of sources and L_{pt} is the total pressure resulting by the addition of all the sources [54].

Table 3-2 shows the final specifications of the sensor, the mathematical model presented for the center deflection (equation

$$\left[C_s f_s(v)\frac{\widetilde{E}h}{a^4}\right]w_o^3 + \left[\begin{array}{c} C_r\frac{\sigma_o h}{a^2} + C_b\frac{12D}{a^4} \\ -\frac{\varepsilon_o V^2}{2a}\left(\frac{2a}{d_o^3} + 0.197\frac{a^{0.25}}{d_o^{2.25}}\right)\end{array}\right]w_o$$
$$-\left[P_M + \frac{\varepsilon_o V^2}{2a}\left(\frac{a}{d_o^2} + 0.1576\frac{a^{0.25}}{d_o^{1.25}}\right)\right] = 0$$

$$\textbf{(3.2))}$$

was used to find the deflection due to the V_{ac} applied to the CMUT, this value was used in the relation (3.34) to find the value of the output pressure of a single CMUT, then using equation (3.41) the output pressure is converted from Pa to dB to finalize use the formula (3.42) to calculate the total output pressure generated by the sensor.

Knowing that in air ultrasound at a frequency of 40 kHz loses 0.06dB for every 30 cm that the wave travels due to absorption in the air [53] we can calculate the pressure received from the echo signal in the sensor after to move around the 10 meters. This value is used as the incoming external mechanical pressure P_M in the equation

$$\left[C_s f_s(\nu) \frac{\widetilde{E} h}{a^4} \right] w_o^3 + \left[\begin{array}{c} C_r \frac{\sigma_o h}{a^2} + C_b \frac{12D}{a^4} \\ - \frac{\varepsilon_o V^2}{2a} \left(\frac{2a}{d_o^3} + 0.197 \frac{a^{0.25}}{d_o^{2.25}} \right) \end{array} \right] w_o - \left[P_M + \frac{\varepsilon_o V^2}{2a} \left(\frac{a}{d_o^2} + 0.1576 \frac{a^{0.25}}{d_o^{1.25}} \right) \right] = 0$$

(3.2) to

find the center deflection that will be used in the relation (3.40) to find the output current.

Table 3-2 Final Sensor Design Specifications

Parameter	Value	Unit
Number of CMUTs per tier	1600	--
Total number of CMUTs in the array	40000	--
Total Pressure Generated by the Array	0.965	KPa
Pressure at 5 m distance	0.860	KPa
Pressure of the echo signal (after 10 m)	0.766	KPa
Output Current per Tier (with the echo signal pressure)	2.0277	nA
Output Current of the Array (with the echo signal pressure)	50.69	nA
Unbiased CMUT capacitance	6.91	fF
Unbiased Tier Capacitance	11.05	pF
Unbiased Sensor Capacitance	276.4	pF

In order to simulate the beamforming capability of the design, the array factors and dimensions have been plotted using polar plots. Figure 3-5 shows the beam shape for the non-planar array.
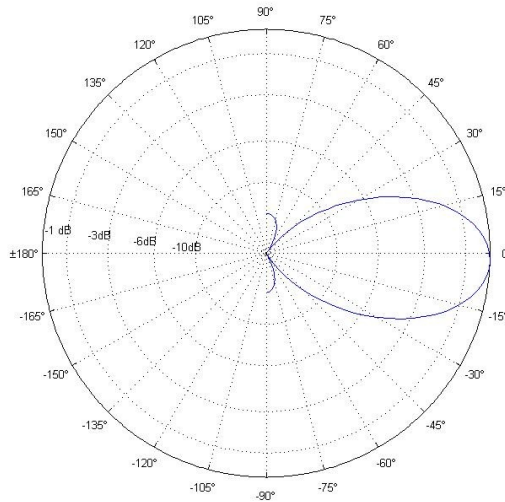
**Figure 3-5 Non-Planar Array Beam Shape**

A highly accurate method to analytically characterize the capacitance change for square-diaphragm CMUTs subject to both acoustic and electrical pressure has been presented. The method includes a new deflection shape function, multilayer diaphragm load-deflection characteristics, and fringing field capacitance models. The method also accounts for the contribution of the dielectric properties of the diaphragm structural material and also the insulation layer used on the bottom electrode to prevent electrical break down. The new deflection shape function has been developed based on the thin plate theory and is applicable to both small- and large-deflection cases. The model can help in improving the design methodology for CMUTs.

4   CHAPTER 4

DESIGN VERIFICATION

This chapter presents the FEA result of key static device parameters and comparing them with analytical results to verify the design process. The key parameters are: diaphragm static deflection, resonant frequency, pull-in voltage, center deflection change and capacitance change of the CMUT.

The analytical pull-in voltage has been calculated using relation (3.37). The pull-in voltage has also been determined by 3-D electromechanical FEA using Intellisuite[TM]. The 3-D FEA result characterizing the pull-in phenomenon is shown in Figure 4-1 a) and b). Table 4-1 presents a comparison of the analytical pull-in voltage and FEA simulation results.
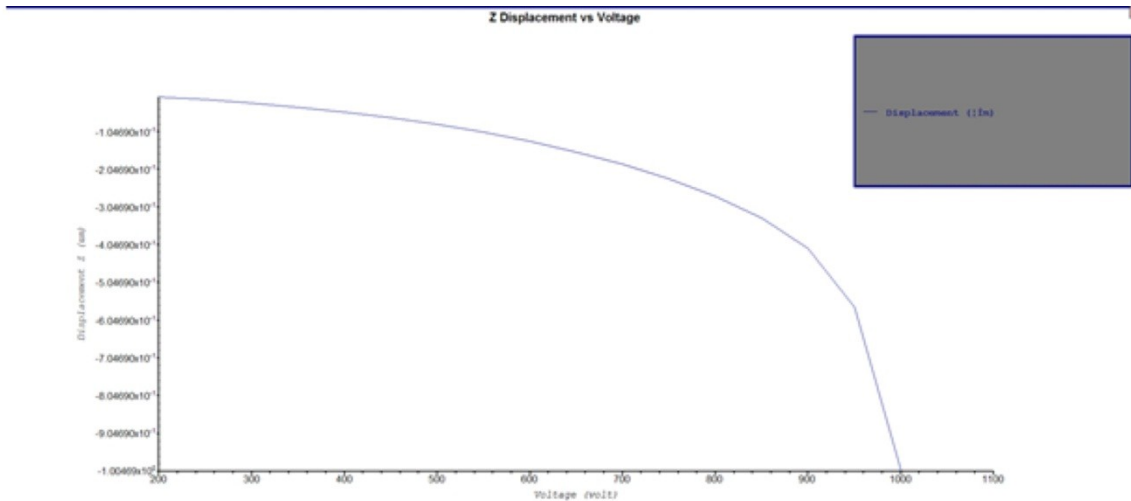
a)
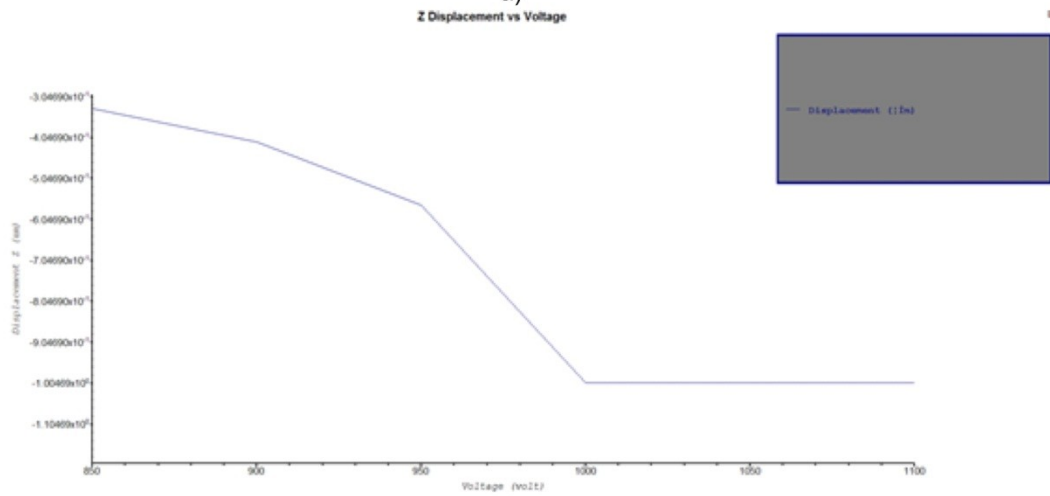
b)

Figure 4-1 FEA displacement vs voltage graph.

Table 4-1 Pull-in Voltage Comparison Table

Pull-in Voltage Calculated	Pull-in Voltage FEA	Difference
978.72 V	951 V	2.8%

The analytical resonant frequency has been calculated using relation (3.35). The resonant frequency has also been determined by 3-D electromechanical FEA using Intellisuite^TM. The 3-D FEA result for the resonant frequency is shown in Figure 4-2. Table 4-2 presents a comparison of the analytical pull-in voltage and FEA simulation results.
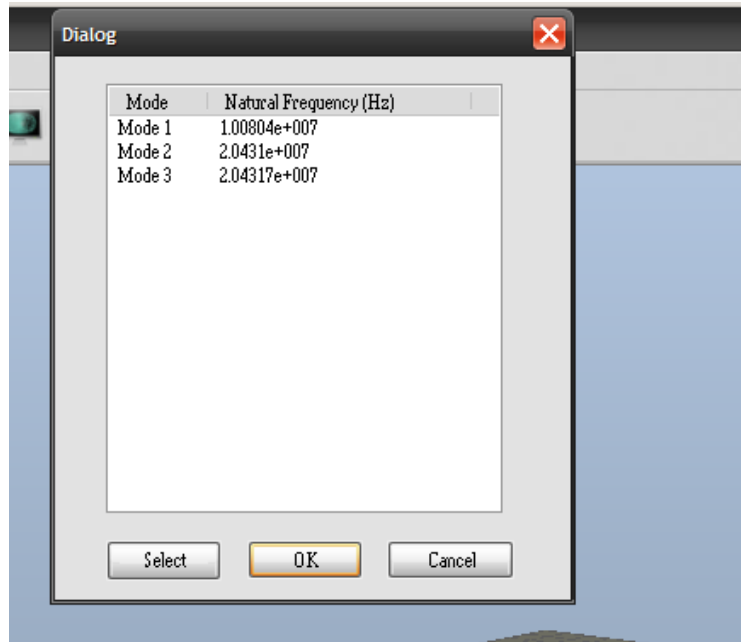
Figure 4-2 Resonant Frequency from FEA

Table 4-2 Resonant Frequency Comparison Table

Resonant Frequency Calculated	Resonant Frequency FEA	Difference
9.6 MHz	10.08 MHz	5%

The new analytical model developed for capacitance change calculation and deflection profile calculation has been verified using 3D Thermoelectromechanical module of IntelliSuite™. Table 4-3 shows a comparison of the values simulated and calculated for different bias voltages, a third column is added where the capacitance has been calculated without considering the

fringing fields the difference is around 10%. Figure 4-3 and Figure 4-4 shows the relation between capacitance and applied voltage using the developed model with and without fringing fields, whereas Figure 4-5 shows the relation between the center deflection and applied voltage. Both the results have been verified by FEA simulation and are in excellent agreement with the model developed. These results show that the effect of applied voltage can't be neglected while calculating either capacitance change or deflection profile.

Table 4-3 CMUT capacitance comparison table

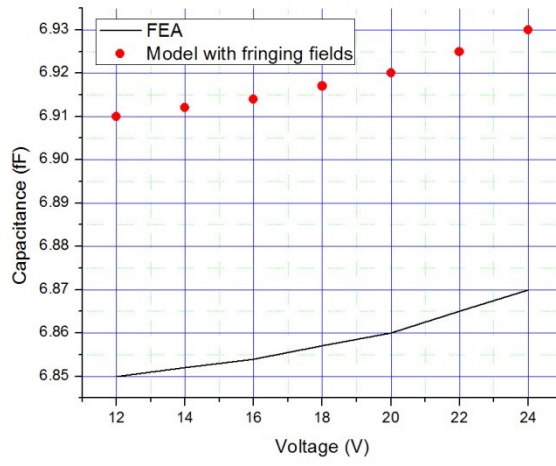| Bias voltage (v)	Capacitance FEA (fF)	Capacitance with fringing fields (fF)	Capacitance without fringing fields (fF)	Variation
12	6.85	6.91	6.219	11 %
14	6.852	6.912	6.2899	9 %
16	6.854	6.914	6.2226	10 %
18	6.857	6.917	6.29447	9 %
20	6.86	6.92	6.2972	9 %
22	6.865	6.925	6.2325	10 %
24	6.87	6.93	6.3063	8 %

Figure 4-3 Capacitance vs voltage (with fringing fields)
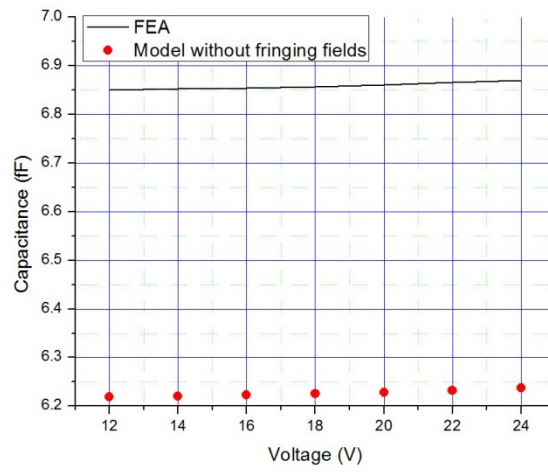

Figure 4-4 Capacitance vs voltage (without fringing fields)
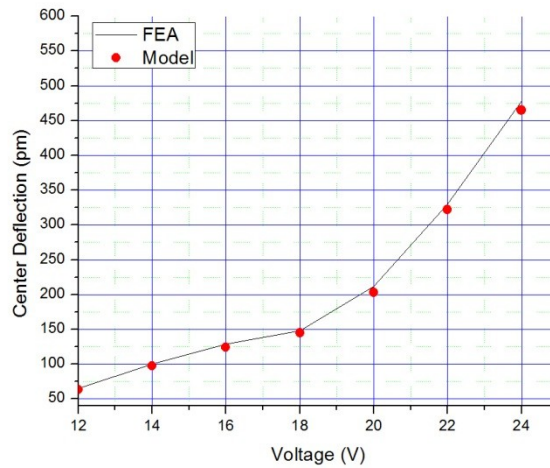
Figure 4-5 Center Deflection vs voltage

4.1   *Simulink Model*

The performance of the CMUT as modeled in Figure 3-3 can be obtained accurately using Simulink (The MathWorks, Inc., Natick, MA). First order model is computationally efficient and reaches very good accuracy which is a derivation of the parallel plate actuator model represented in [55].

The block diagram of the Simulink model for a CMUT is shown in Figure 4-6. It includes a CMUT transmission subsystem, AC and DC voltage inputs, and displacement and pressure outputs. The subsystem is shown in Figure 4-7, comprehend an electrostatic force subsystem (Figure 4-8) and a CMUT membrane subsystem(Figure 4-9). The membrane velocity is converted to output pressure by multiplying the air impedance (loading impedance of the medium). The electrostatic force subsystem transfers input voltage to electrostatic force. The whole system is built based on Equation (3.25).
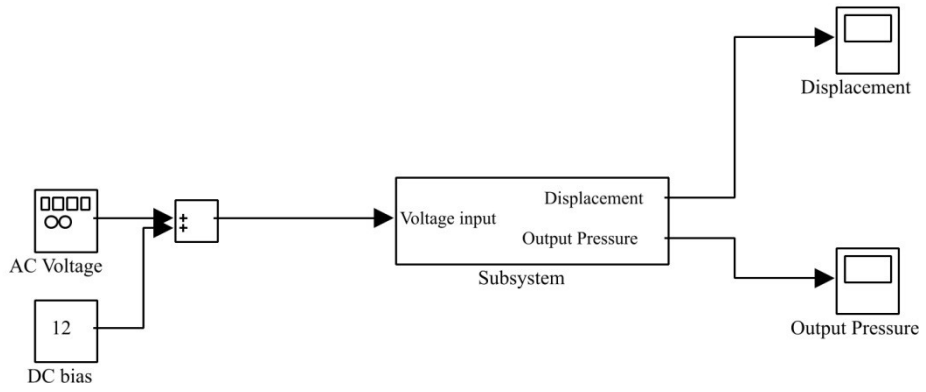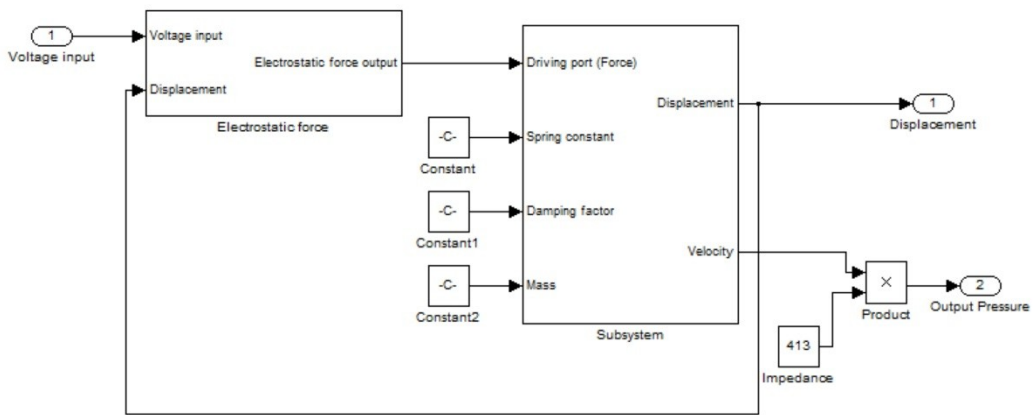
Figure 4-6 Simulink model of a CMUT

Figure 4-7 Simulink model of a CMUT (subsystem)
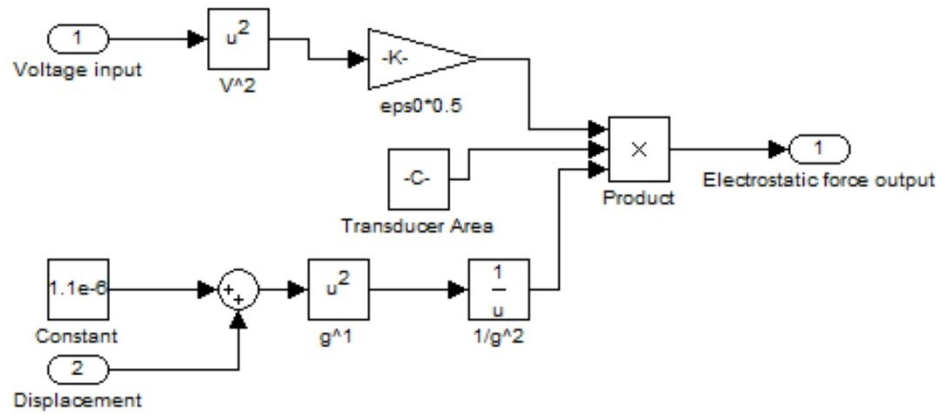
74

Figure 4-8 Simulink diagram of an electrostatic force subsystem in Fig 3-10
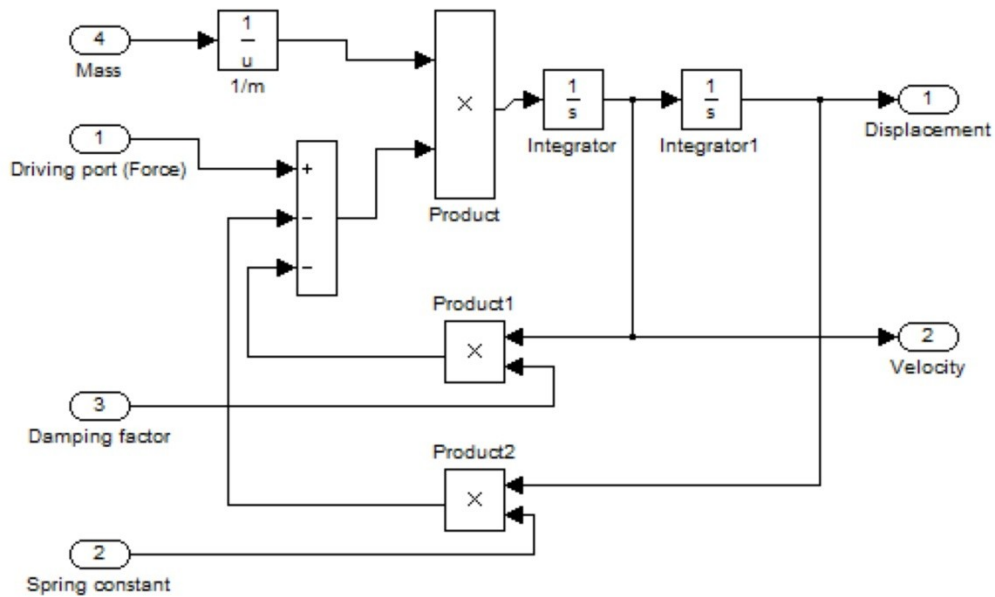

Figure 4-9 Simulink diagram of a CMUT membrane in Fig 3-10

The specifications stated in Table 3-1 has been introduced into the Simulink model. Figure 4-10 shows the output pressure generated from the CMUT, once is steady the value differs only by 10 % from the value obtained using the Equation (3.34). Figure 4-11 shows the displacement obtained with the applied voltage in the system.
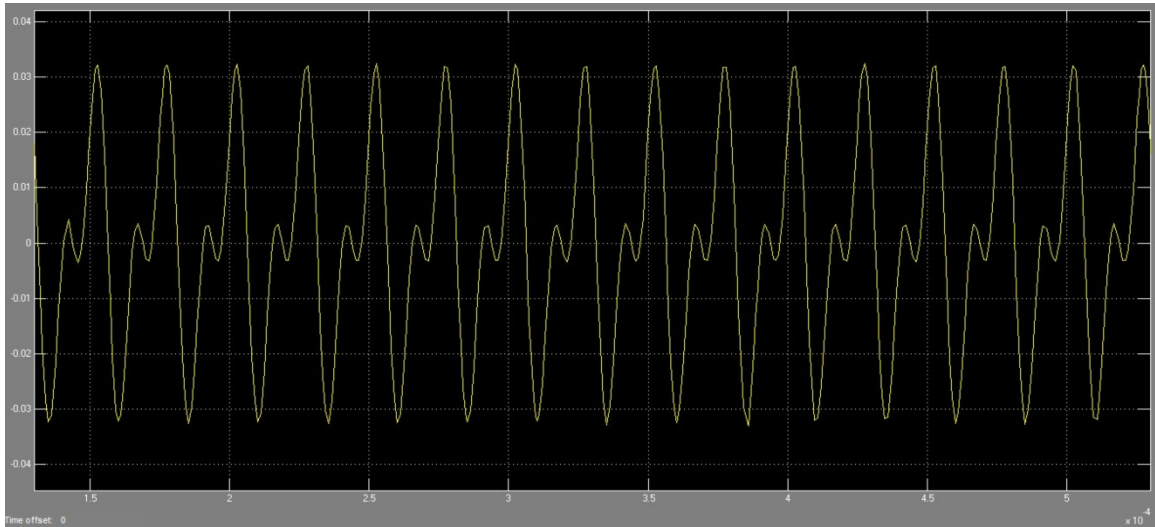
75

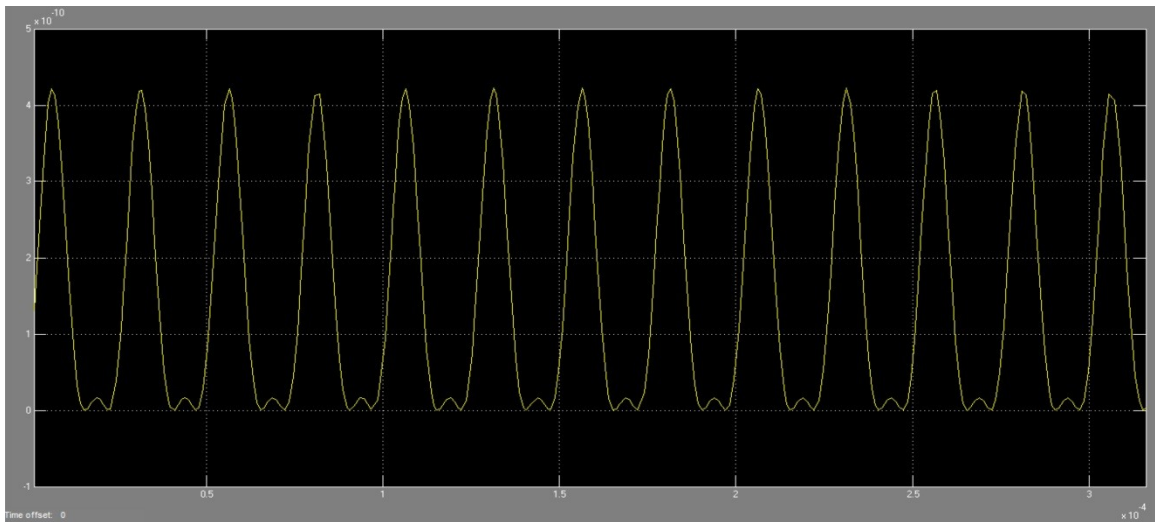Figure 4-10 Output pressure from CMUT (Simulink model)

Figure 4-11 Membrane displacement from CMUT (Simulink model)

The model has accurately simulated the behaviour of the CMUT, and shows the dynamic characteristics of the CMUT. The simulated results are in reasonably good agreement with analytical results.

In this chapter the mathematical model presented in chapter 3 to find the center deflection, capacitance, resonant frequency and pull in voltage has been verified through FEA simulations using IntelliSuite™, the results are in excellent agreement with the analytical ones.

A Simulink model has been presented to accurately model the performance of the CMUT; this model is used to precisely find the output pressure of the CMUT and the membrane displacement generated by applying a bias voltage and Vac signal to the CMUT. The Simulink model is simple to implement, and it takes only seconds on a personal computer (PC) to finish a simulation.

5   CHAPTER 5

FABRICATION

This chapter presents the fabrication methodology develop to fabricate Capacitive Micromachined Ultrasonic Transducers (CMUT). The methodology incorporates the detailed step by step of the fabrication process, used materials, process type, and conceptual cross sectional view of the process.

5.1   *Array Fabrication Details*

This section describes the fabrication process for the 5 meter non-planar array design as described previously. The array is designed to have 5 sensing surfaces in both the *x* and *y* direction. The 25 sensing surfaces are fabricated on SOI wafers. After dicing, the sensing surface dies are to be assembled using a VeroWhitePlus Fullcure835 (Plastic) structure to ensure appropriate elevations are met. VeroWhitePlus Fullcure835 is used to avoid any possibly short circuit during the packaging process.

It has been calculated that the total height of the system is 3.36 mm, considering that the array will have 7 elevations each level will be 0.48mm height, the total dimensions of the array are shown in Figure 5-1.
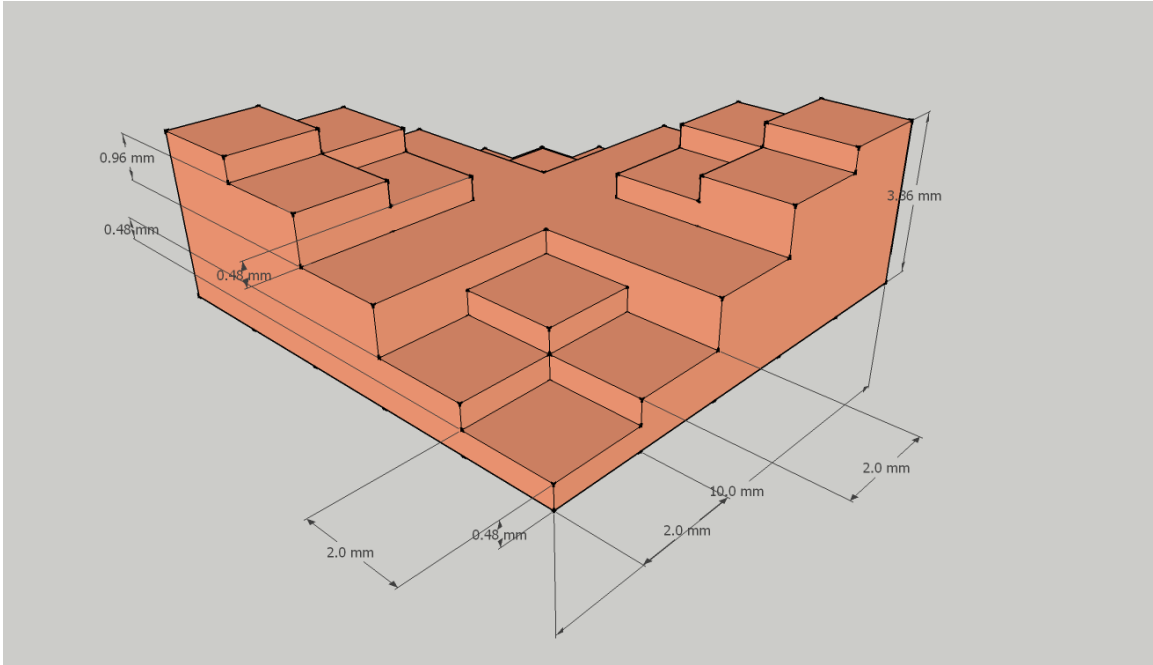
Figure 5-1 Final dimensions for the non-planar array

The methodology to build the array consist of collocate a sensing surface with 40x40 CMUT in each of the level of the VeroWhitePlus Fullcure835 non-planar structure, this surface will be adhered to the plastic using silver epoxy EPO-TEK ® EE 129-4, silver epoxy is used in order to have a conductive surface to connect the bottom electrode of the CMUT. The total area of each level is 2 mm x 2 mm, considering that each tier area is 1.87 mm x 1.87 mm there is 130 μm of free space, this space was used to wire bonding with gold the bottom electrodes together since the bottom electrode are adhered with the silver epoxy which is a conductor then all the bottom electrodes will be connected in parallel. Then, all the top electrodes were wire bonding together using gold, Figure 5-2 shows a conceptual image of this process.
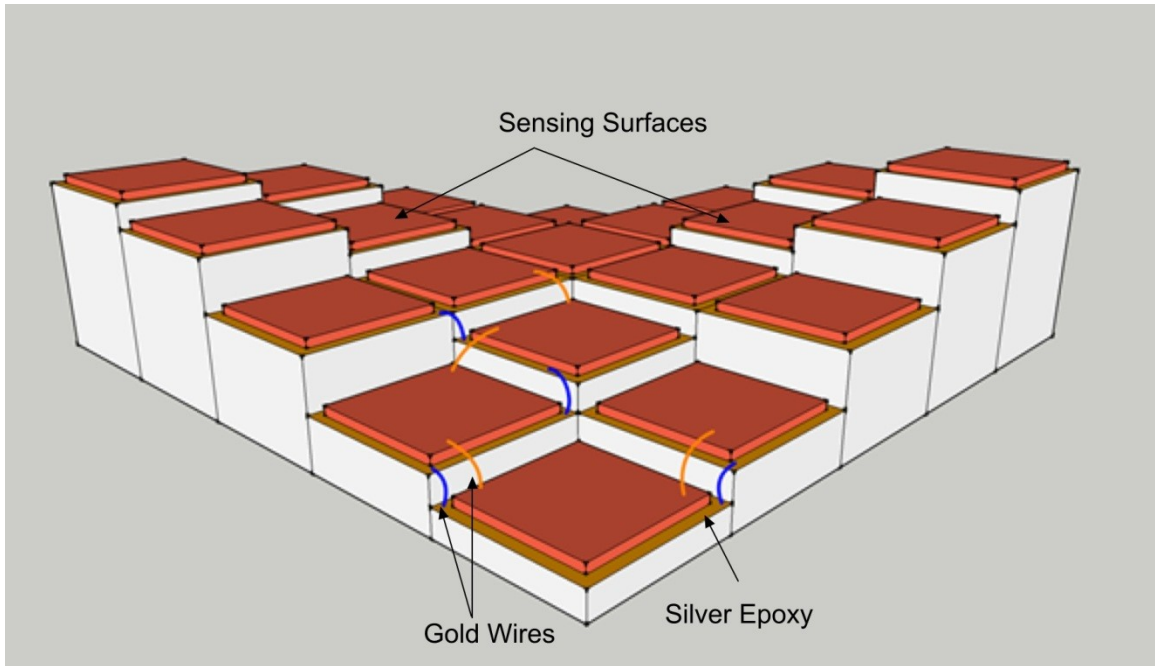
Figure 5-2 Conceptual Image of non-planar array

SOI wafers possess several advantages for the fabrication process such as:

- Higher quality factor

- Lower value of residual stress

- Thickness uniformity

- Reduction in fabrication process complexity

- Reduction in fabrication steps

- Lower number of masks

- Reduction of cost [56]

It has been demonstrated that SOI based CMUT are a viable option and show excellent agreement between experimental and analytical values [50], however measurements done in previous sensors shows a discrepancy between capacitance change due to bias voltage, this effect can be seen in the Figure 5-3.
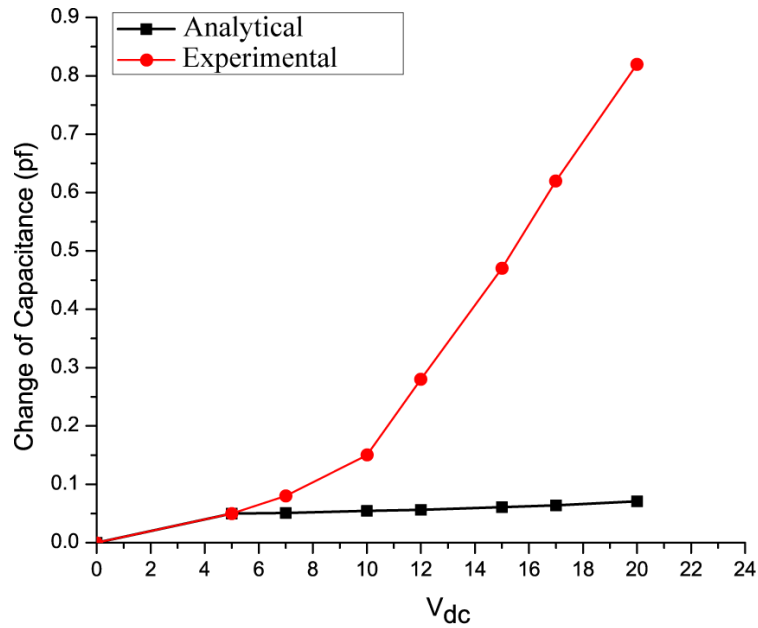
Figure 5-3 Comparison between analytical and experimental values [23]

From Figure 5-3 it is evident that the measured capacitance change values are 4 to 10 times higher than the theoretical values. Since similar data were obtained with multiple test runs [23], it can be concluded that some dielectric charging phenomena occurs in the CMUT as the bias voltage is increased or decreased to effect a fluctuation in the capacitance values. The actual physics of this dielectric charging is still under investigation and sufficient mathematical models are yet to be developed to capture the complex physical phenomenon that takes place when a dielectric material like silicon dioxide is exposed to a strong electric field, possible causes for this can be:

- Covalent bonds of SiO_2 which is affected by dielectric polarization and charging

- Temperature effects the charge traps, and provides enough energy to dipoles to overcome potential barriers and randomize their orientation [57]

81

- Strong electrostatic field causes excessive charges to get trapped due to silicon dangling bonds [58]

- Low temperature deposition leads to formation of silicon clusters inside silicon dioxide layer, causing leakage and charge trap interfaces.

- Absorbed moisture particles due to relative humidity also causes leakage, and discrepancy in capacitance readings [59]

In order to attack this problem an two solutions have been formulated, one is to have vacuum in the cavity in order to keep all the moisture particles out of the cavity and the other one is to include an insulation layer in top of the bottom electrode to avoid that any leakage currents can reach the bottom electrode, however it's imperative to have an insulation layer with low level of ionic contaminants in order to prevent leakage currents and charge traps. As was mentioned in Chapter 3 the material that covers those requirements is the BCB.

Taking that in consideration a novel SOI based fabrication process has been developed using BCB to BCB bonding.

5.2   Fabrication Process Steps

The characteristics of the SOI wafer to be used are listed in the following table:

Parameter	Specification(s)
Diameter	100±0.2 mm
Crystal Orientation	<100>
Overall Thickness	352±5 µm
Front side finished	Polished
Back Side Finished	Nanogrind @2000mesh
Device Layer	
Thickness	2±0.7 µm
Type/Dopant	n/Sb
Resistivity	<0.01 -0.2 Ohm-cm
Handle wafer	
Thickness	500±25 µm
Type/Dopant	n/Phos
Resistivity	<1-10 Ohm-cm
Buried Oxide	
Thermal Oxide	1±5% µm

Step 1: Thin of the top layer of the SOI.

Since the SOI wafer has an initial thickness of 2 µm, it's necessary to thin the top layer until the 0.8 µm thickness is reached. The silicon was etched at constant parameters of a 100-W bias powers, a 40-Sccm (Standard Cubic Centimeters per Minute) CF4 flow rate, 50 mTorr pressure at a 58 *nm/min* rate. Figure 5-4 shows this procedure.

Figure 5-4 Step 1: Thinning SOI Wafer

Step 2: BCB Coating.

Then a 900 *nm* BCB layer thickness will be spin deposited over the silicon wafer [60]using a 1 nanometer layer thickness of AP3000 as an adhesive. To prepare the surface for BCB coating, the adhesion promoter solution is applied to the surface of the substrate, which is then spun dry. The surface is immediately ready for BCB coating. AP3000 is designed for spin coating [61]. The BCB is diluted in a 2:1 ratio by weight (2 Cyclotene 3022-46, 1 Mesitylene) and spin deposited with a 4550 rpm speed. Figure 5-5 shows this procedure
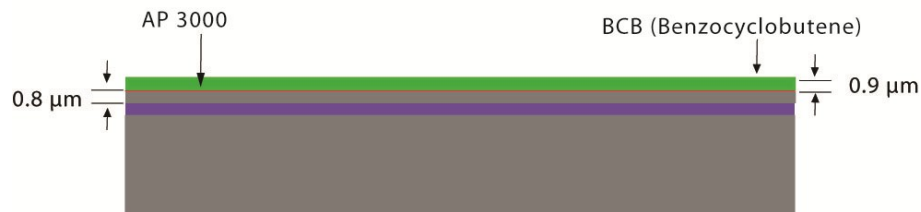

Figure 5-5 BCB Coating (900 nm)

Step 3: BCB Curing and patterning.

The BCB layer once deposited is cured under nitrogen flow during 5 hours starting with a ramp to 150 ˚C, stay 15 min at 150 ˚C, the temperature is increased to a ramp to 210 ˚C staying 40 min at that temperature then is cooling down to less than 150 ˚C. In the Figure 5-6 can be seen that the BCB thickness shrinks from 880nm before curing to about 800 *nm* after curing.
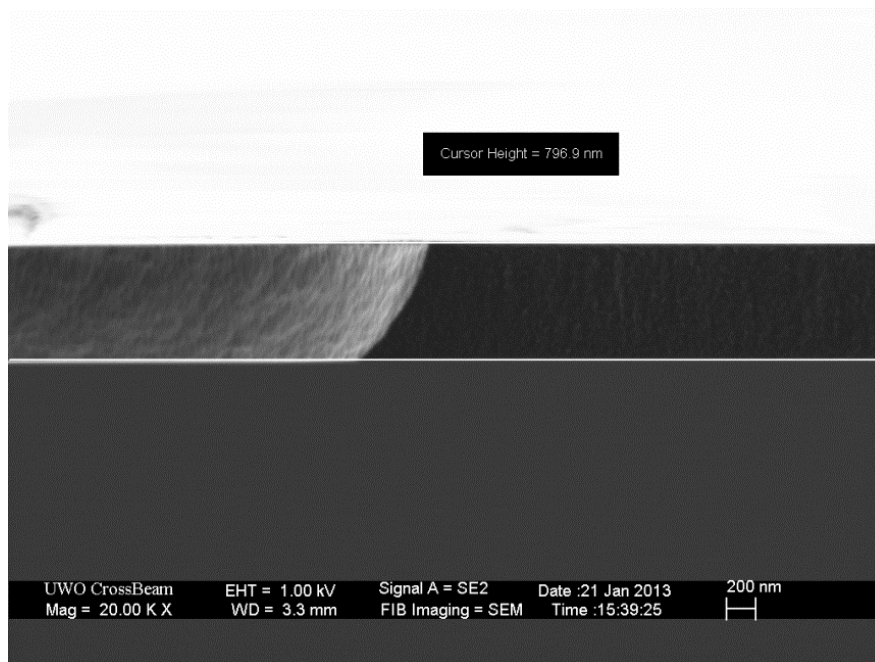

Figure 5-6 SEM Image showing BCB layer thickness

The BCB needs to be etch in order to form the cavity of the CMUT, Shipley 1805 photoresist layer is spin deposited, after soft baking of the photoresist (150 ˚C) the etching is done at constant parameters of a 300-W RF power, a 22.5 Sccm CF_4 and 90 Sccm O_2 flow rate, 50 mTorr pressure , the BCB etching rate was *295 nm/min* , for the photoresist 85 *nm/min* and for the Silicon 85 *nm/min.* A close-up of the mask developed to perform the etching is show in Figure 5-7, the rest of the mask has the same dimensions that the diagram shown in Figure 3-4. Figure 5-8 shows this procedure.

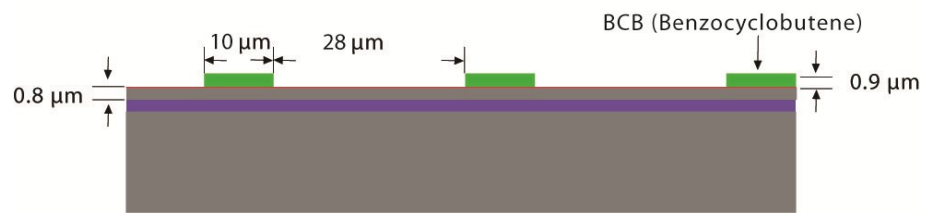**Figure 5-7 Close-up of the mask used to create the cavity**
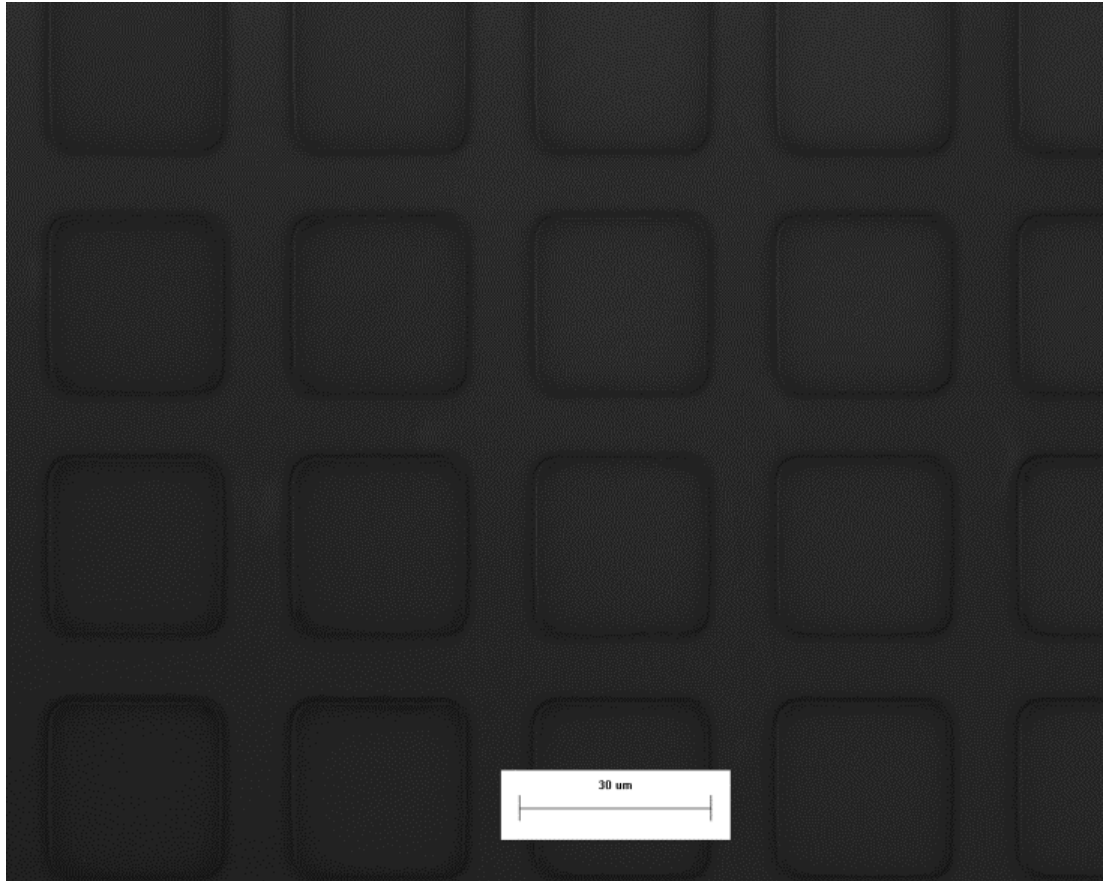

Figure 5-8 Making cavity in BCB layer

Step 4: Coating handle wafer with BCB.

In order to perform the bonding its necessary to coat the handle wafer with a thin 200 nm layer of BCB, the BCB is spin deposited as in the step 2, the BCB is diluted in a 5:16 ratio by weight (2 Cyclotene 3022-46, 1 Mesitylene) and spin deposited with a 2530 rpm speed . Figure 5-10 shows this procedure.

Figure 5-10 BCB coating (200 nm)

Step 5: Bonding

The next step is to bond the two wafers together using the BCB as the bonding agent, being this the most critical part of the process several trials were performed to finally reach the final parameters to successfully bond the wafers. Three recipes were tried, the cure process was found to be critical in the process, following the 3 iterations were done to bond the wafers.

For the first one the BCB curing recipe for cavities under nitrogen flow (time required 4-5 h) starts with a ramp to 150 ˚C, stay 15 min at 150 ˚C, the temperature is increased to a ramp to 210 ˚C staying 40 min at that temperature then is cooling down to less than 150 ˚C. The BCB bonding recipe under vacuum (time required 4-5 h) starts with a ramp to 150 ˚C, stay 15 min at 150 ˚C, the temperature is increased to a ramp to 210 ˚C staying 2 h at 210 ˚C then is cooling down to less than 150 ˚C. Figure 5-11 shows a SEM image of the resulting bonding the white spots represent the areas where the bonding was not performed properly.
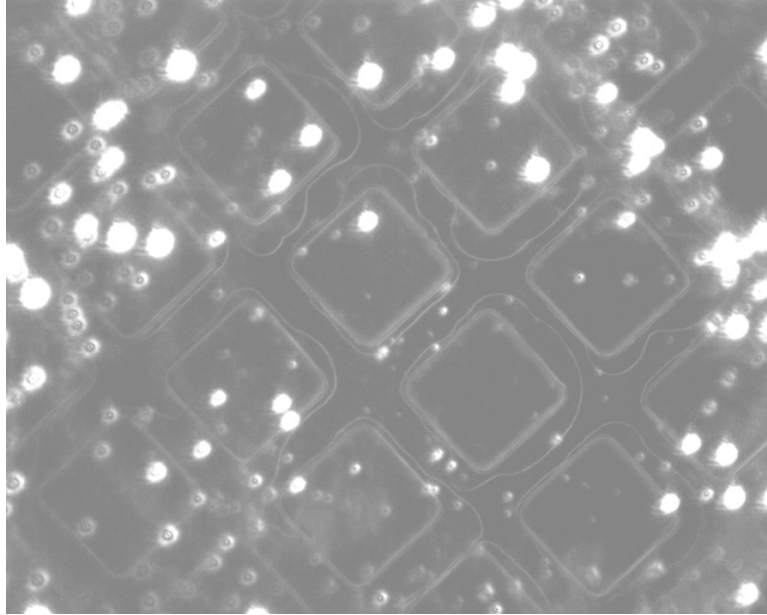
For the second one the BCB curing recipe for cavities under nitrogen flow (time required 4-5 h) starts with a ramp to 150 ˚C, stay 2 hour at 150 ˚C, then is cooling down to less than 150 ˚C. The BCB bonding recipe under vacuum (time required 5-6 h) starts with a ramp to 150 ˚C, stay 15 min at 150 ˚C, the temperature is increased to a ramp to 210 ˚C staying 2 h at 210 ˚C then is cooling down to less than 150 ˚C. Figure 5-12 shows a SEM image of the resulting bonding, the shape of the mask used can be easily recognized meaning that the bonding has been performed correctly.
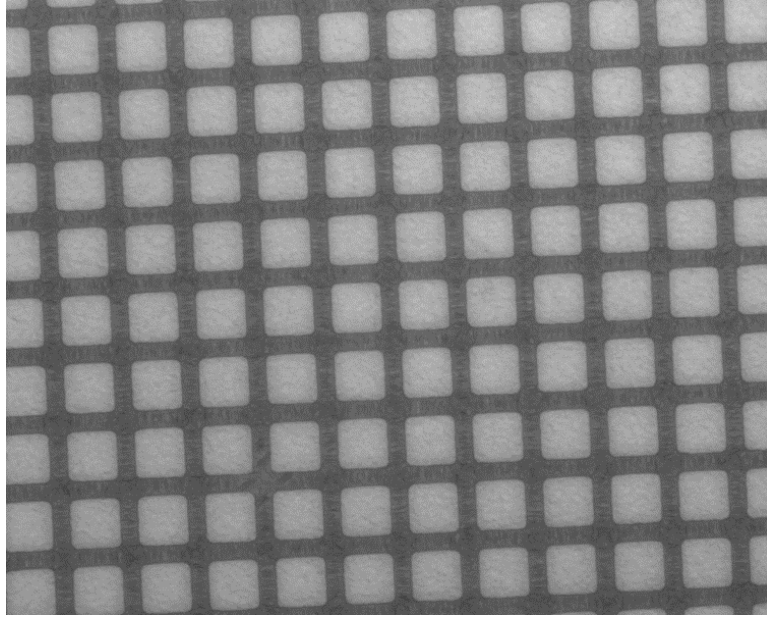
Figure 5-12 SEM image BCB bonding (second iteration)

For the third one the BCB curing recipe for cavities under nitrogen flow (time required 3-4 h) starts with a ramp to 190 ˚C, stay 2 h at 190 ˚C, then is cooling down to less than 150 ˚C. The BCB bonding recipe under vacuum (time required 4-5 h) starts with a ramp to 150 ˚C, stay 15 min at 150 ˚C, the temperature is increased to a ramp to 210 ˚C staying 2 h at 210 ˚C then is cooling down to less than 150 ˚C. Figure 5-13 shows a SEM image of the resulting bonding, in this case Pyrex is used, some silicon remained in the glass as can be seen in the picture, however the bonding process has been performed properly and the shape of the tier remain.
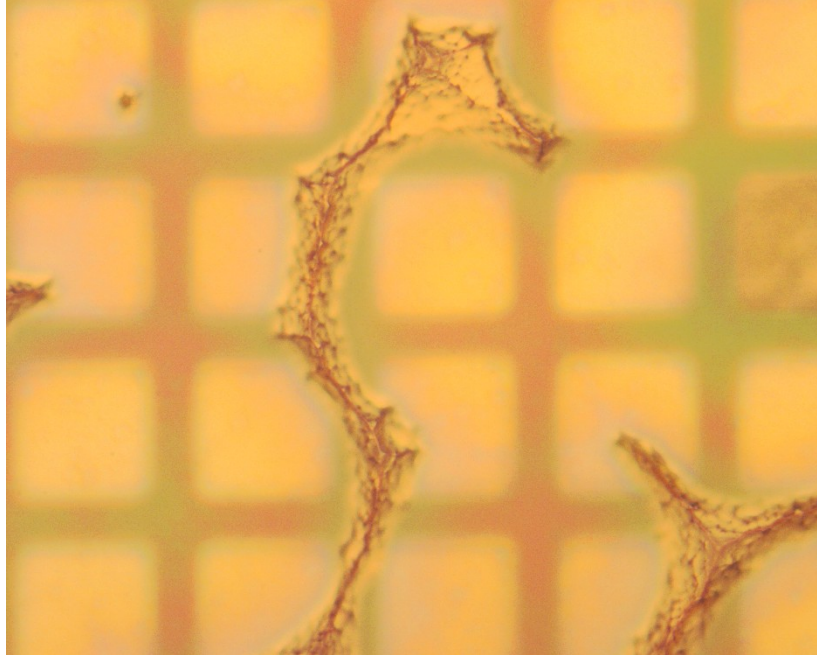
0.8 µm

1.1 µm

Figure 5-14 BCB Bonding

Step 6: Removing of the sacrifice silicon handle and BOX layers

It's necessary to thinning the substrate wafer, in order to do so the following recipe has been followed , using SF_6 and high power plasma for remove only 450 µm out of 500 µm of silicon, the etch rate is 4 – 6 µm/min and the Silicon to Oxide etch selectivity is around 45, using 20% hot KOH (for the remaining 50 µm) at a etch rate of 1.5   µm/min and the silicon to oxide etch selectivity with this process is around 275.Figure 5-15 shows the final product after this process,

91

in the Figure 5-16 a SEM image can be seen of the CMUTs after the silicon removal its clear that the shape of the membranes has been kept and that the deflection that is seen is due to the atmospheric pressure.

Figure 5-15 CMUT after removal of silicon and BOX layers

Figure 5-16 SEM image of the CMUTs after silicon removal

Step 6: PAD metallization

The final step is to electron beam evaporate a 100 nm thickness layer of gold to metalized the device and a 1 μm metal pad to apply the voltage to the top electrode. Figure 5-17 shows a conceptual cross section of the metalized CMUT.
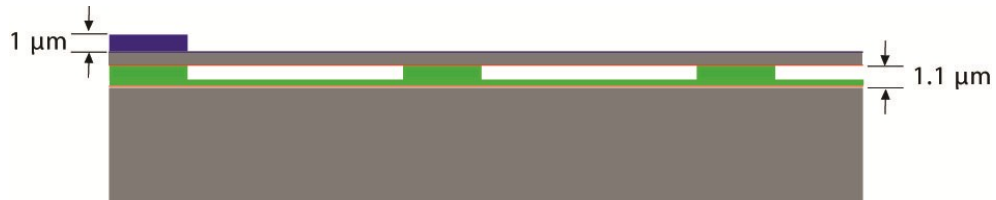
5.3   Packaging Process

After the fabrication and dicing of the CMUTs, the CMUTs will be assembled using a non-planar VeroWhitePlus Fullcure835 (Plastic) structure to obtain proper vertical offset to realize the desired discretized hyperbolic paraboloid geometry. Before this point the 3D structure was already placed over a 68 Ceramic PGA package (SSM P/N CPG06863). The 3D structure was designed using CAD software, to then be 3D printed in VeroWhitePlus Fullcure835 for the company PROTO3000 3D Engineering Solutions, Figure 5-18 shows an image of the generated model. VeroWhitePlus Fullcure835 was chosen as the material for the non-planar array to keep proper isolation between the two different voltage levels, which is the biasing voltage and the ground level. Figure 5-19 shows the non-planar array already printed out.
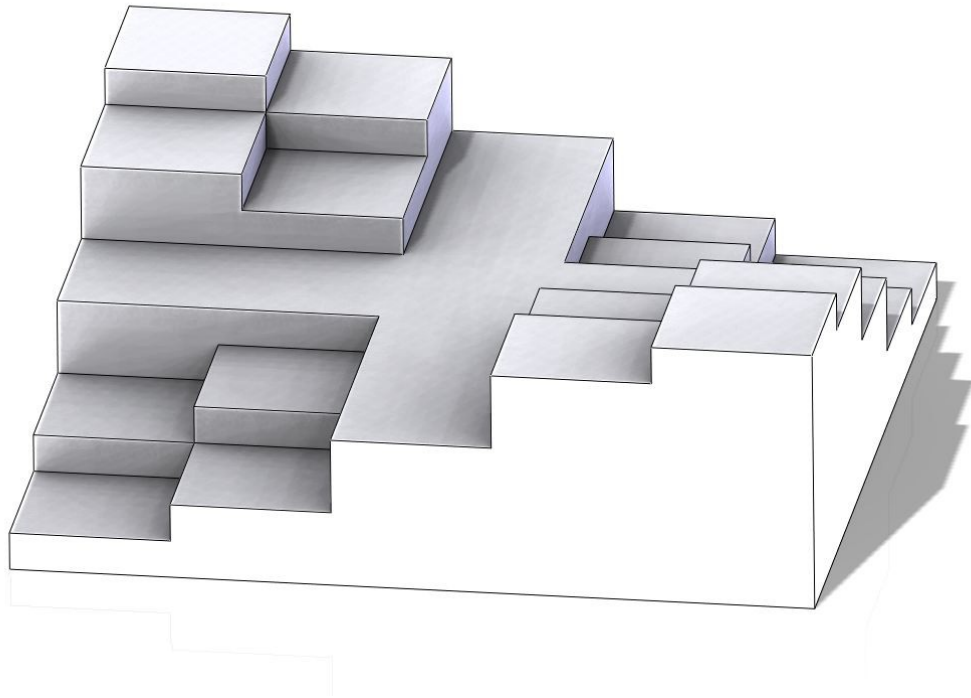
Figure 5-18 Generated CAD model for the non-planar array

Figure 5-19 Verowhite plus Fullcure835 3D printed non-planar array

The CMUTs will be deposited over the structure using silver epoxy EPO-TEK ® EE 129-4 as adhesive, silver epoxy EPO-TEK ® EE 129-4 is a room temperature cure, silver-filled epoxy, designed for making electrical connections in circuit assembly, semiconductor, and LCD applications.

Conductive epoxy is used to provide a conductive connection between the handle layer of SOI base CMUT and the rest of the CMUTs through wire gold bonding so that a common electrical base point is obtained for all the dies instead of having separate grounding for each of them. Same procedure will be follow to connect all the top electrodes together through gold wire bonding as shown in Figure 5-2. This also helps in reducing the pin connection complexity.

After assembling, individual sensing surfaces are electrically connected to the bonding pads of a commercially available PGA-68 package using gold bonding wires.

The package serves to integrate all of the components required for a system application in a manner that minimizes size, cost, mass and complexity. The package provides the interface between the components and the overall system. The three main functions of the MEMS package are mechanical support, protection from the environment, and electrical connection to other system components.

The array has a dimension of 10.0x10.0 mm and a PGA-68 package has a cavity size of 12.0 x 12.0 mm. Thus a commercially available PGA-68 package will meet the requirements for the CMUT microarray. Figure 5-21 shows the PGA-68 package details, the pins where the voltage must be applied are indicated in the figure. Another requirement of packaging is the definition of bonding pads. In order to ease the assembly and interconnection process, each of the sensing

surfaces has been fabricated to have a 100 µm wide strip (as shown in Figure 5-20). Thus the

gold bonding wires can be bonded at any location on the strip. The final device is shown in

Figure 5-22.

100 µm

Figure 5-20 Bonding pad

Top Electrode Connection
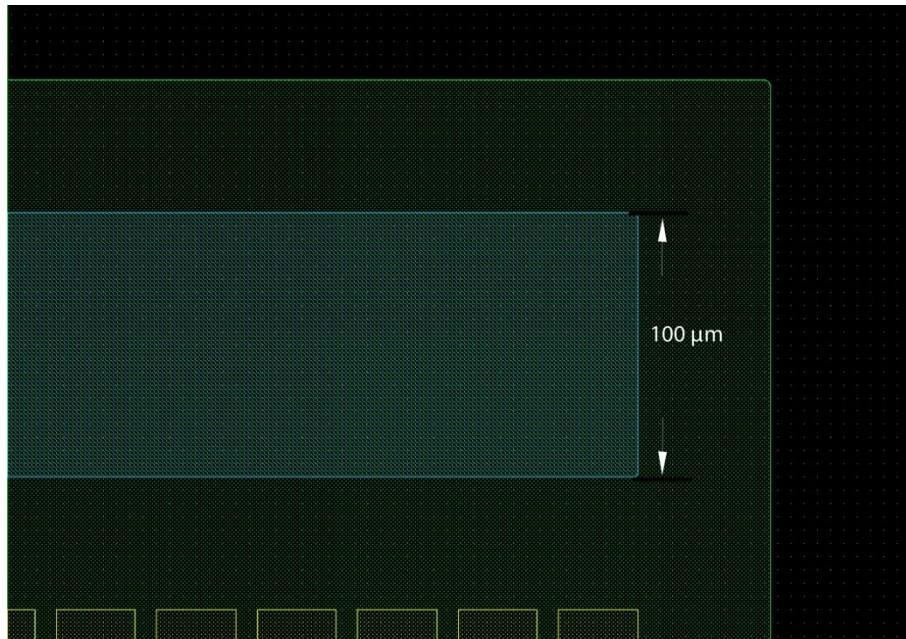
Bottom Electrode Connection (ground)
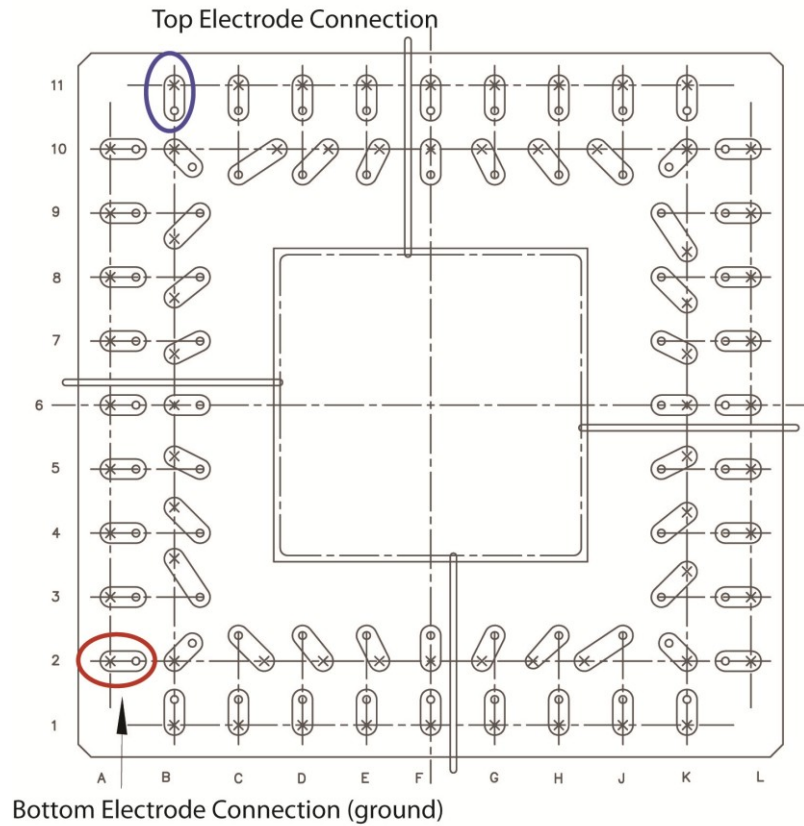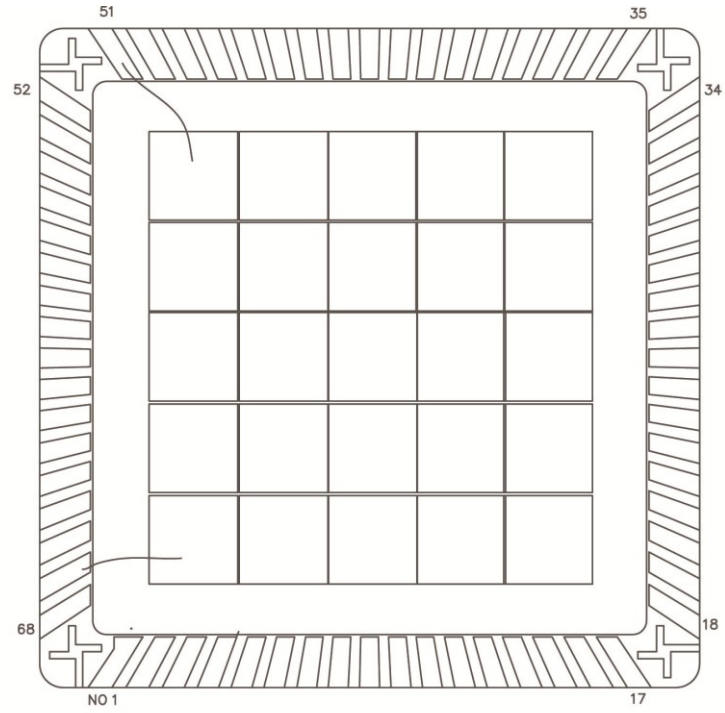
Figure 5-21 68 Ceramic package connections
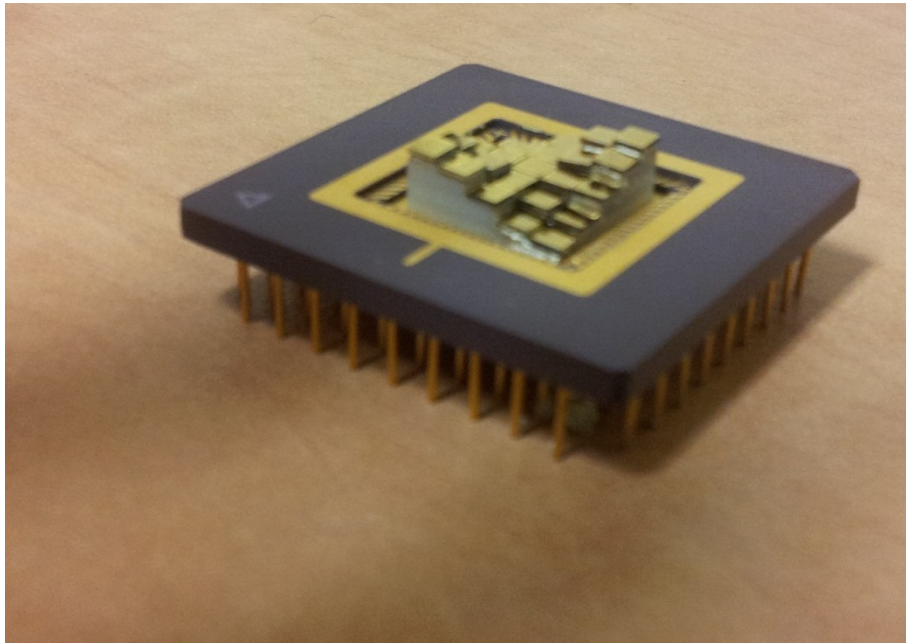
Figure 5-22 Non-planar CMUT array

The sensor has been tested following the parameters from Table 3-2 , the equipment used to tested is shown in Figure 5-23, Figure 5-24 and Figure 5-25 shows the signal transmitted from the sensor using a microacoustic BAT-3 detector as the receiver [62]. At a distance of 30 cm the signal received has an amplitude of 300 mv peak to peak while at a distance of 15 cm the signal amplitude is 800 mv peak to peak.
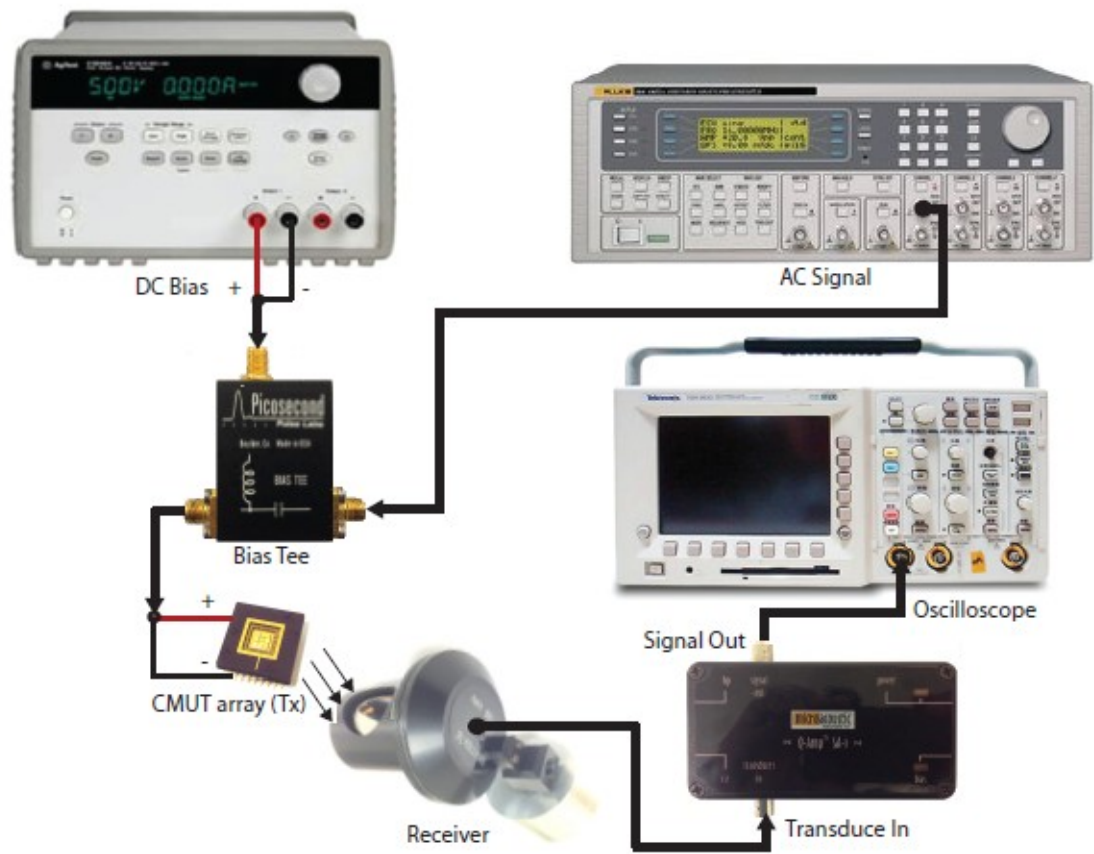
Figure 5-23 Set up to test the sensor
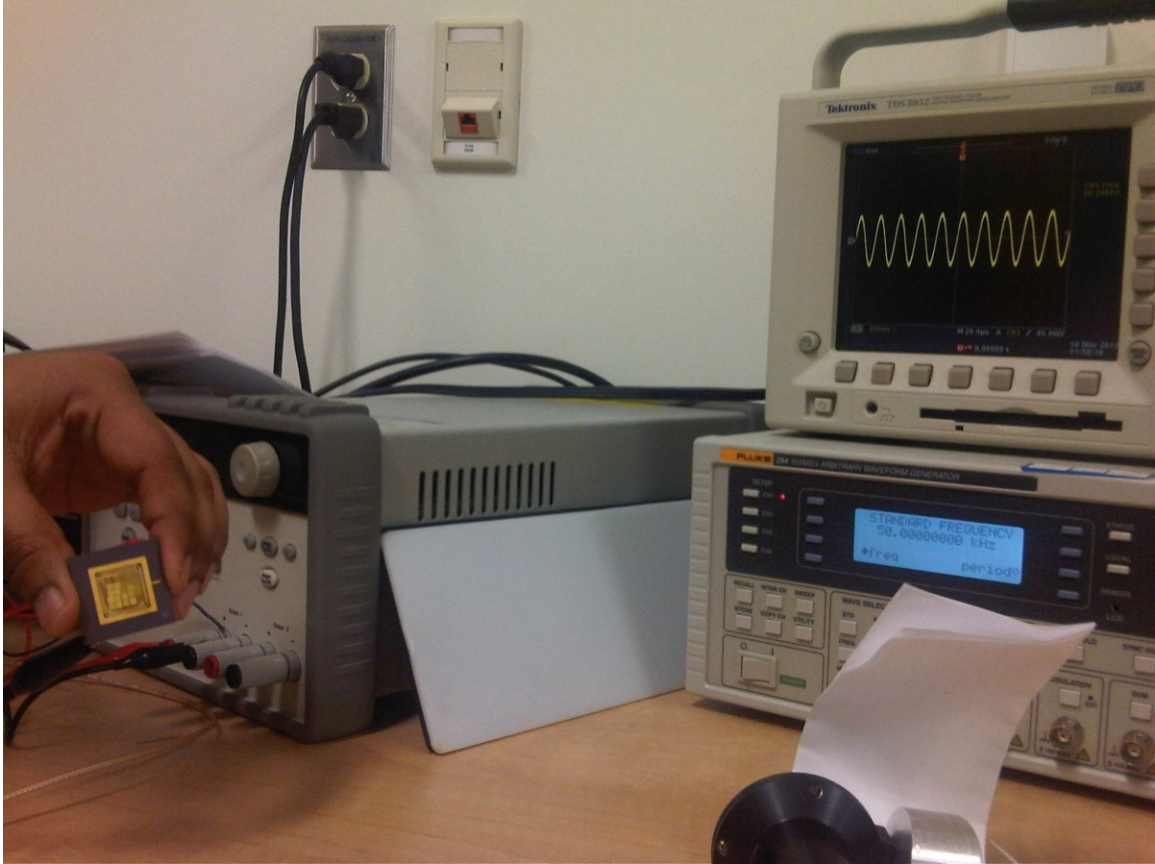
Figure 5-24 Receiver output 30 cm away from sensor
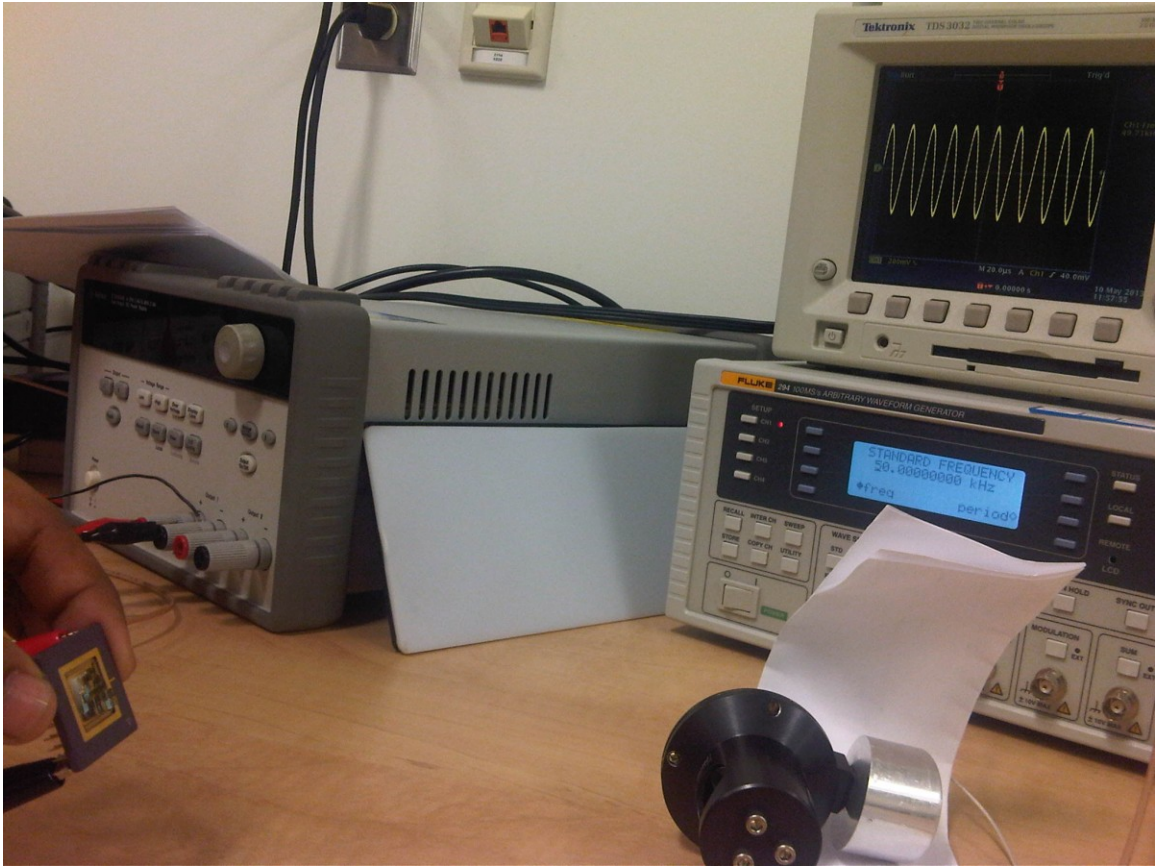
Figure 5-25 Receiver output 15 cm away from sensor

In this chapter the fabrication process for the non-planar array has been presented, for the first time BCB has been used in the fabrication of a CMUT, an easy to implement method for the packaging has been also presented. This new packaging method involved the use of a VeroWhitePlus Fullcure835 (Plastic) structure to avoid any possibility of a short circuit between the tiers. The sensor has been tested with an easy to implement set up, the preliminary results are encouraged however further measurements need to be carried out.

6   CHAPTER 6

CONCLUSIONS AND FUTURE DIRECTIONS

A successful design, simulation, and fabrication of a 5 meter range non-planar Capacitive Micromachined Ultrasonic Transducer (CMUT) array for automotive collision avoidance that can provide a constant bandwidth broadband beamforming capability without any microelectronic signal processing has been carried out in this thesis.

Current beamforming solutions involve microelectronics based complex algorithms, making these systems more complex and subject to processing time latency. A discrete hyperbolic paraboloid shaped array which has intrinsic beamforming capabilities and hence forth can provide a cheaper and less complex solution for real time applications as compared to the currently available solutions. The scientific approach of this research work is based on the previous work [13]. The developed robust, high sensitivity, low power, batch manufacturable sensor microarray has the geometry of a discretized hyperbolic paraboloid surface and capacitive sensing has been used as the transduction mechanism to realize a cost-effective proposal for a 5 meter range non-planar CMUT for automotive collision avoidance.

As part of the mathematical model of the array a highly accurate method to analytically characterize the capacitance change for square-diaphragm CMUTs subject to both acoustic and electrical pressure has been presented. The method includes a new deflection shape function, multilayer diaphragm load-deflection characteristics, and fringing field capacitance models. The method also accounts for the contribution of the dielectric properties of the diaphragm structural material and also the insulation layer used on the bottom electrode to prevent electrical break down.

A mathematical model to calculate the output pressure and as a consequence the maximum distance the sensor can be reach has been presented, together with this model a way to find the output current delivered for the sensor has been presented, every tier can generate 2.0277 nA with the echo signal received, since the sensor has a total number of 25 tiers the total output current generated is 50.69 nA.

From previous work has been shown that trapped charges buried in silicon dioxide layer (ionic contamination), dipole polarization, and interfacial polarization, causes a high variation when comparing analytical, FEA and experimental values of capacitance in a given device [50]. Additionally leakage current through a higher dissipative factor dielectric and conduction through the air also effects a higher change of capacitance while causing heating. Consequently, an alternative dielectric with a lower ionic contamination and dissipative factor as Benzocyclobutene (BCB) was investigated and proposed as the dielectric spacer for CMUTs.

BCB has many figures of merit [52] such as low dielectric constant, a low electrical current loss factor at high frequencies, low moisture absorption, low cure temperature, high degree of planarization, low level of ionic contaminants, high optical clarity, good thermal stability, excellent chemical resistance, and good compatibility with various metallization systems. Lower ionic contamination prevents leakage currents and charge traps, which is an important factor in MEMS devices.

A VeroWhitePlus Fullcure835 (Plastic) structure has been used to realize the hyperbolic paraboloid discretized structure, silver epoxy EPO-TEK ® EE 129-4 was used to adhere the individual tiers over the non-planar structure proving to be an excellent option.

The non-planar array was tested showing excellent results, however further measurements need to be performed and also to prepare a more complete testing set up needs to be done in order to fully test the sensor and to find its limitations and capabilities.

6.1   *Future directions*

Being the packaging process one of the main concerns in MEMS technology an acoustical cover over the package is desired. This cover will be able to improve the ruggedness of the device and make it less prone to ambient tampering, contamination but the performance requirements for such a cover make it a research challenge.

Also more measurements need to be done in the sensor in order to fully characterize its static and dynamic behaviour and to find its limitations and capabilities.

Wider beamwidth can be achieved by exploring the mathematical model presented in Chapter 2, Figure 6-1 shows a 70˚ beamwidth achieved by changing alpha and lambda, further investigations are needed to fully understand the limitations of the model and find new and innovated applications.
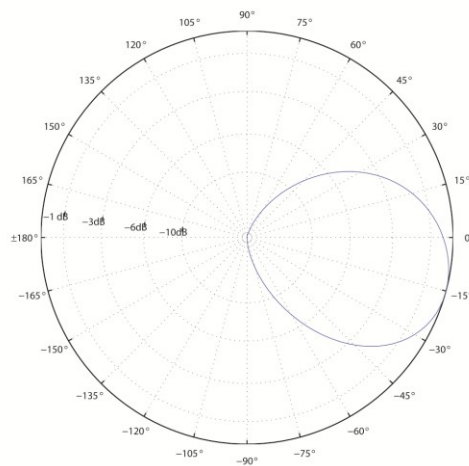

Figure 6-1 Beamwidth 60 degrees

REFERENCES

[1] United States National Highway Traffic Safety Administration, General Motors Corportation, Delphi Delco
     Electronics Systems Washington, National Highway Traffic Safety Administration 2000, "Automotive Collision
     Avoidance System Field Operational Test, First Annual Report, June 1999-June 2000," 15 December 2000.
     [Online]. Available:
     http://www.nhtsa.gov/Research/Crash+Avoidance/Office+of+Crash+Avoidance+Research+Technical+Publications.
     [Accessed 23 March 2013].

[2] European Commission, Commission of the European Communities, "REGULATION (EC) No 661/2009 OF THE
     EUROPEAN PARLIAMENT AND OF THE COUNCIL," 31 July 2009. [Online]. Available: http://eur-
     lex.europa.eu/LexUriServ/LexUriServ.do?uri=OJ:L:2009:200:0001:0024:en:PDF. [Accessed 23 March 2013].

[3] European Commision, Commision of the European Communities, "Proposal for a Regulation of the European
     Parliament and of the Council concerning Type-approval requirements for the general safety of motor vehicles,"
     23 May 2008. [Online]. Available:
     http://ec.europa.eu/enterprise/sectors/automotive/files/safety/sec_2008_1908_en.pdf. [Accessed 22 March
     2013].

[4] Highway Loss Data Institute, "Status report, special issue crash avoidance," 3 July 2012. [Online]. Available:
     http://www.iihs.org/externaldata/srdata/docs/sr4705.pdf. [Accessed 22 March 2013].

[5] Bosch Group, "Bosch Media Service," Bosch Media Service, 27 April 2010. [Online]. Available: http://www.bosch-
     presse.de/presseforum/details.htm?txtID=4570&locale=en. [Accessed 22 March 2013].

[6] Ford Motor Company, "FORD'S LATEST SAFETY BRAKETHROUGH – COLLISION WARNING WITH BRAKE SUPPORT –
     COMING IN 2009," Ford Motor Company, April 2009. [Online]. Available:
     http://media.ford.com/article_display.cfm?article_id=29188. [Accessed 20 March 2013].

[7] Honda Media Service, "Collision Mitigation Brake System (CMBS)," 18 June 2003. [Online]. Available:
     https://techinfo.honda.com/rjanisis/pubs/om/JA0606/JA0606O00325A.pdf. [Accessed 22 March 2013].

[8] J. J. Breuer, A. Faulhaber, P. Frank and S. Gleissner, "Real World Safety Benefits of Brake Assistance Systems," in
     ESV Conference, Lyon, 2003.

[9] M. Kiyoka, Y. Yamada, M. Iyoda, S. Koike, T. Kawasaki and M. Tokuda, "Development of Rear Pre-Crash Safety
     System for Rear-End Collisions," *Toyota Tech Rev.,* vol. 55, no. 1, pp. 84-89, 2006.

[10] CMC Microsystems, "Advanced and Affordable Collision Avoidance Capability with Commercial Potential," 14
     October 2012. [Online]. Available:
     http://www.cmc.ca/~/media/AboutCMC/SuccessStories/All/Advanced_and_affordable_Chowdhury-EN-LO.pdf.

[Accessed 22 March 2013].

[11] A. Sinjari and S. Chowdhury, "MEMS automotive collision avoidance radar beamformer," in *IEEE International Symposium on Circuits and Systems, ISCAS*, Seattle, 2008.

[12] M. Meloche and S. Chowdhury, "Design of a MEMS Discretized Hyperbolic Paraboloid Geometry Ultrasonic Sensor Microarray," *IEEE Trans. Ultra. Ferro. And Freq. Control,* vol. 55, no. 6, pp. 1363-1372, 2008.

[13] M. Meloche, "A MEMS Non-Planar Ultrasonic Microarray," Master's thesis, University of Windsor, 2007.

[14] H. Yongli, Z. Xuefeng, E. Hggstrom, A. Ergun, C. Ching-Hsiang and B. Khuri-Yakub, "Capacitive micromachined ultrasonic transducers with piston-shaped membranes: fabrication and experimental characterization," *Ultrasonics, Ferroelectrics and Frequency Control, IEEE Transactions on,* vol. 56, no. 1, pp. 136-145, 2009.

[15] Ergun, S. Arif, Y. Goksen G. and B. T. Khuri Yakub, "Capacitive Micromachined Ultrasonic Transducers: Theory and Technology," *Journal of Aerospace Engineering,* vol. 16, no. 2, pp. 76-84, 2003.

[16] J. X.C., O. Oralkan, F. Degertekin and B. Khuri-Yakub, "Characterization of one-dimensional capacitive micromachined ultrasonic immersion transducer arrays," *Ultrasonics, Ferroelectrics and Frequency Control, IEEE Transactions on,* vol. 48, no. 3, pp. 750-760, 2001.

[17] F. Hunt, Electroacoustics: The Analysis of Transduction, and Its Historical Background, New York: Acoustical Society of America, 1982.

[18] B. Khuri-Yakub, F. Degertekin, X.-C. Jin, S. Calmes, I. Ladabaum, S. Hansen and X. Zhang, "Silicon Micromachined Ultrasonic Transducers," in *IEEE International Ultrasonics Symposium*, Sendai, 1998.

[19] A. Savoia, G. Caliano and M. Pappalardo, "A CMUT probe for medical ultrasonography: from microfabrication to system integration," *Ultrasonics, Ferroelectrics and Frequency Control, IEEE Transactions on,* vol. 59, no. 6, pp. 1127,1138, 2012.

[20] H. Yongli, E. Haeggstrom, Z. Xuefeng, A. Ergun and B. Khuri-Yakub, "Capacitive micromachined ultrasonic transducers (CMUTs) with isolation posts," in *Ultrasonics Symposium, 2004 IEEE*, Montréal, 2004.

[21] J. Chen, X. Cheng, C.-C. Chen, P.-C. Li, J.-H. Liu and Y.-T. Cheng, "A Capacitive Micromachined Ultrasonic Transducer Array for Minimally Invasive Medical Diagnosis," *Microelectromechanical systems, Journal of,* vol. 17, no. 3, pp. 599,610, 2008.

[22] S. D. Senturia, Microsystem Design, New York: Springer, 2001.

[23] J. Hernandez Aguirre, T. Zure and S. Chowdhury, "Capacitance Measurments of an SOI Based CMUT," in *LASCAS 2013, 2013 IEEE 4th Latin American Symposium on Circuits and Systems*, Cusco, 2013.

[24] Y. Huang, A. Sanli Ergun, E. Hæggström, M. H. Badi and B. T. Khuri Yakub, "Fabricating Capacitive Micromachined Ultrasonic Transducers With Wafer-Bonding Technology," *Microelectromechanical Systems, Journal of,* vol. 12, no. 2, pp. 128-137, 2003.

[25] S. Beeby, MEMS Mechanical Sensors, Artech House on Demand, 2004.

[26] M. J. Madou, Fundamentals of microfabrication: the science of miniaturization, CRC Pressl Llc., 2002.

[27] J. Morris, "Broad-band constant beam-width transducers," *Journal of Sound and Vibration,* vol. 1, no. 1, pp. 28-40, 1964.

[28] Van Veen, B. D. and K. M. Buckley, "Beamforming: A versatile approach to spatial filtering," *ASSP Magazine IEEE 5.2,* no. 2, pp. 4-24, 1988.

[29] J. Morris, Broad-band Echo-Location, Ph. D. dissertation, England: University of Birmingham, 1964.

[30] J. Stewart, Calculus: early transcendentals, Thomson Brooks/Cole, 2010.

[31] B. S. and M. D., "Safety Code 24 - Guidelines for the safe Use of Ultrasound: Part II - Industrial and Commercial Applications," 1991. [Online]. Available: http://www.hc-sc.gc.ca/ewh-semt/pubs/radiation/safety-code_24-securite/index-eng.php. [Accessed 17 April 2013].

[32] R. Seip, B. Adamczyk and D. Rundell, "Use of Ultrasound in Automotive Interior Occupancy Sensing: optimum frequency, beamwidth and SNR from empirical data," in *Ultrasonics Symposium*, Lake Tahoe, 1999.

[33] R. Ervin, J. Sayer, D. LeBlanc, S. Bogard, M. Mefford, M. Hagan, Z. Bareket and C. Winkler, "Automotive Collision Avoidance System Field Operational Test Report: Methodology and Results," No. HS-809 900, 2005.

[34] H. Elgamel, "Closed-form expression of the relationships between stress, membrane deflection, and resistance change with pressure in silicon piezoresistive pressure sensors," *Sensors and Actuators A: Physical,* vol. 50, no. 1, pp. 17-22, 1995.

[35] S. Timoshenko and S. Woinowsky-Krieger, Theory of Plates and Shells, New York, NY: McGraw-Hill, 1959, pp. 396-424.

[36] M. Van Der Meijs and J. Fokkema, "VLSI circuit reconstruction from mask topology," *INTEGRATION the VLSI journal,* vol. 2, no. 2, pp. 85-119, 1984.

[37] R. Mosaddequr, S. Abbas and S. Chowdhury, "A simple capacitance calculation formula for MEMs capacitive sensors with square diaphragms," in *Circuits and Systems and TAISA Conference, 2009. NEWCAS-TAISA'09. Joint IEEE North-East Workshop on*, Touluse, 2009.

[38] D. Maier-Shneider, J. Maibach and E. Obermeier, "A new analytical solution for the load-deflection of square

membranes," *Microelectromechanical Systems Journal of,* vol. 4, no. 4, pp. 238-241, 1995.

[39] A. Nettles, "Basic mechanics of laminated composite plates," National Aeronautic Space Administration, Washington, DC, 1994.

[40] M. Rahman, J. Hernandez and S. Chowdhury, "An improved analytical method to design CMUTs with square diaphragms," *Ultrasonics, Ferroelectrics and Frequency Control, IEEE Transactions on,* vol. 60, no. 4, pp. 834, 845, April 2013.

[41] S. Way, "Uniformly loaded, clamped, rectangular plates with large deflection," in *Proc. Fifth Int. Cong. Appl. Mech*, Cambridge, 1938.

[42] B. Samuellevy, "Square plate with clamped edges under normal pressure," Report No. 740-National Advisory Committee for Aeronautics, 1942.

[43] X. Ye, J. Zhang, Z. Zhou and Y. Yang, "Measurement of Young's modulus and residual stress of micromembranes," in *Micro Machine and Human Science, 1996., Proceedings of the Seventh International Symposium IEEE*, 1996.

[44] H. E. A. Elgamel, "A simple and efficient technique for the simulation of capacitive pressure transducers," *Sensors and Actuators A: Physical,* vol. 77, no. 3, pp. 183-186, 1999.

[45] S. Tong, D. D.B., C. H.N. and A. Fenster, "A Three Dimensional Ultrasound Prostate Imaging System," *Ultrasound in medicine & biology,* vol. 22, no. 6, pp. 735-746, 1996.

[46] G. Hayward and A. Gachagan, "An Evaluation of 1–3 Connectivity Composite Transducers for Air-coupled Ultrasonic Applications," *The Journal of the Acoustic Society of America,* vol. 99, pp. 2148-2157, 1996.

[47] M. Haller and B. T. Khuri Yakub, "A Surface Micromachined Electrostatic Ultrasonic Air Transducer," *Ultrasonics, Ferroelectric and Frequency Control, IEEE Transactions on,* vol. 43, no. 1, pp. 1-6, 1996.

[48] P.-C. Hsu, H. Mastrangelo and K. Wise, "A High Sensitivity Polysilicon Diaphragm Condenser Microphone," in *Micro Electro Mechanical Systems, MEMS 98. Proceedings., The Eleventh Annual International Workshop on*, 1998.

[49] A. S. Ergun, B. Temelkuran and E. Ozbay, "A New Detection Method for Capacitive Micromachined Transducers," *Ultrasonics, Ferroelectrics and Frequency Control, IEEE Transactions on,,* vol. 48, no. 4, pp. 932-942, 2001.

[50] T. Zure, Characterization of a CMUT array, Windsor: Master's Thesis, University of Windsor, 2011.

[51] T. Zure and S. Chowdhury, "Fabrication and measurements of dynamic response of an SOI based non-planar CMUT array," *Microsystem technologies,* vol. 18, no. 5, pp. 629-638, 2012.

[52] S. Ying Hung, P. Garrou, J.-H. Im and D. M. Scheck, "Benzocyclobutene-based polymers for microelectronics," *Chemical innovation,* vol. 31, no. 12, pp. 40-47, 2001.

[53] B. Bosnjakovic, P. Czersky, M. Faber, D. Harder and J. Marshall, Interim guidelines on limits of human exposure to airborne ultrasound.

[54] "The Engineering Tool Box," [Online]. Available: http://www.engineeringtoolbox.com/adding-decibel-d_63.html. [Accessed 20 November 2012].

[55] X. Zhuang, Capacitive micromachined ultrasonic transducers with through-wafer interconnects, ProQuest, 2008.

[56] SOI Industry Consortium, official website, "Annual Report," March 2009. [Online]. Available: http://www.soiconsortium.org/about-soi/economics-benefits.php. [Accessed April 2013].

[57] G. Papaioannou and R. Plana, "Physics of Charging in Dielectrics and Reliability of Capacitive," *Advanced Microwave and Millimeter Wave Technologies Semiconductor ,* pp. 275-302, 2010.

[58] X. Yuan, Z. Peng, J. Hwang, D. Forehand and C. Goldsmith, "Acceleration of dielectric charging in RF MEMS capacitive switches," *Device and Materials Reliability, IEEE Transactions on,* vol. 6, no. 4, p. 556–563, 2006.

[59] H. R. Shea, A. Gasparyan, H. Bun Chan, S. Arney, R. E. Frahm, D. Lopez , S. Jin and R. P. McConell, "Effects of electrical leakage currents on MEMS reliability and performance," *Device and Materials Reliability, IEEE Transactions on,* vol. 4, no. 2, pp. 198-207, 2004.

[60] S. Stankovic, D. Van Thourhout, G. Roelkens, R. Jones, J. Heck and M. Sysak, "Die-to-Die Adhesive Bonding for Evanescently-Coupled Photonic Devices," *ECS Transactions,* vol. 33, no. 4, pp. 411-420, 2010.

[61] CYCLOTENE Advanced Electronic Resins, "Processing Procedures for BCB Adhesion," CYCLOTENE Advanced Electronic Resins, 2007.

[62] MicroAcoustic Instruments Inc., "Products: BAT's transducers," 2006. [Online]. Available: http://www.microacoustic.com/BAT_species.htm. [Accessed 29 April 2013].

VITA AUCTORIS

Jonathan Hernandez Aguirre was born in 1986 in Durango, Dgo. Mexico, received the B.S. degree in electrical engineering from the Durango Institute of Technology, Mexico, in 2008. From 2008 to 2010, he was with Delphi in the steering systems division, where he was in charge of launching several steering systems. His research interests include capacitive micromachined ultrasound transducers, MEMS, and early crash detection sensors. Currently, Jonathan is a member of the MEMS Lab in Electrical and Computer Engineering at the University of Windsor, Windsor, ON, Canada, and a candidate for the M.A.Sc degree.

- For update information please refer to ca.linkedin.com/pub/jonathan-hernandez-aguirre/2a/501/79/